UAV survey method to monitor~~ing~~ and analyze~~sing~~ geological hazards: The Case study of the mud volcano of Villaggio Santa Barbara, Caltanissetta (Sicily)

Fabio Brighenti[1], Francesco Carnemolla [1], Danilo Messina[3] & Giorgio De Guidi[1 2]

[1] Department of Biology, geology and Environmental Sciences, University of Catania, Catania, 95129, Corso Italia 55 – 57, Italy

[2] CRUST-Interuniversity Center for 3D Seismotectonics with territorial applications - UR-UniCT, Catania, 95129, Corso Italia 55 – 57, Italy

[3] Indipendent Researcher

Correspondence to: Giorgio De Guidi (deguidi@unict.it)

Abstract. All active geological processes determine effects on the soil due to different deformation processes: surface uplift and subsidence, shear lineaments with differential kinematics in relation to the source and the soils involved. Nowadays ~~the~~ remote sensing represents a key tool for the evaluation and monitoring of the natural -hazards. The use of Unmanned Aerial Vehicles (UAVs) in contexts of natural hazard presents three main steps for risk assessment ~~and monitoring~~: pre-post event data acquisition, emergency support and monitoring. The mud volcano of Santa Barbara (Municipality of Caltanissetta, Italy), represents a dangerous site because on 11th August 2008 a paroxysmal event caused serious damage to infrastructures for a range of about 2 km. The main clues of mud volcano paroxysmal events are the uplift and the development of structural features with dimensions ranged from centimetre to decimetre. Here we present a methodology for monitoring of deformation processes that may be precursors of paroxysmal events on the Santa Barbara mud volcano. This methodology is based on i) the data collection, ii) the Structure f~~r~~rom Motion (SfM) processing chain and iii) the M3C2-PM algorithm for the comparison between point clouds and uncertainty analysis with a statistical approach. The objective of this methodology is to detect hazard precursors by monitoring of deformation processes with centimetre precision and a temporal frequency of 1 - 2 months.

1. Introduction

In recent decades, both high-resolution digital photographs and Structure f~~r~~rom Motion (SfM) softwares allowed to generate high-quality topographic information. In geosciences many studies have been dedicated to morphological processes (Castillo et al., 2012; James and Robson, 2012; James and Varley, 2012; Amici et al. 2013b; Casella et al., 2014; Gomez-Gutierrez et al., 2014; James and Robson, 2014b; Lucieer et al., 2014; Ryan et al., 2015; Westoby et al., 2015; Woodget et al., 2015; Eltner et al., 2015; Dietrich, 2016; Smith et al., 2016; Javernick et al., 2016; Walter et al., 2018b; Deng et al. 2019)~~(Amici et al. 2013b; Casella et al., 2014; Castillo et al., 2012; Deng et al. 2019; Dietrich, 2016; Eltner et al., 2015; Gomez-Gutierrez et~~

al., 2014; ~~James and Robson, 2012; James and Robson, 2014b, James and Varley, 2012; Javernick et al., 2016; Lucieer et al., 2014; Ryan et al., 2015; Smith et al., 2016; Walter et al., 2018b; Westoby et al., 2015; Woodget et al., 2015~~). Applications include runoff laboratory trials (Morgan et al., 2017), applied geology (Niethammer et al., 2012; Russell, 2016; Saito et al., 2018), geomorphology (Javernick et al., 2014; Snapir et al., 2014; Dietrich, 2015; Smith and Vericat, 2015; Bakker and

35   Lane, 2016; ~~Balaguer Puig et al., 2017; Dietrich, 2015;~~ Dietrich, 2016 a/b; Mercer and Westbrook, 2016; Pearson et al., 2017; Prosdocimi et al., 2017; Marteau et al., 2016; Balaguer-Puig et al., 2017; Vinci et al., 2017; Heindel et al., 2018; ~~Javernick et al., 2014; Marteau et al., 2016; Mercer and Westbrook, 2016; Pearson et al., 2017; Prosdocimi et al., 2017;~~ Seitz et al., 2018~~; Smith and Vericat, 2015; Snapir et al., 2014; Vinci et al., 2017~~), glaciology (Immerzeel et al., 2017; Piermattei et al., 2016), coastal morphology (James and Robson, 2012; Casella et al., 2016; Brunier et al., 2016~~; James and Robson,

40   2012~~), volcanology (James and Robson, 2012; Bretar et al., 2013; ~~Andaru and Rau, 2019; Bretar et al., 2013; Carr et al., 2018; De Beni et al. 2019; Favalli et al., 2018; Giordan et al., 2017, 2018; James and Robson, 2012;~~ Müller et al. 2017~~;~~ Giordan et al., 2017, 2018; Carr et al., 2018; Favalli et al., 2018; Witt et al. 2018; Andaru and Rau, 2019; Bonali et al. 2019; De Beni et al. 2019) and geophysics (Amici et al., 2013a; Greco et al., 2016; Di Felice et al., 2018~~; Federico et al., 2019~~; ~~Greco et al., 2016;~~ Zahorec et al., 2018; Federico et al., 2019). SfM is commonly used in the cultural heritage field for the

45   3D reconstruction (~~Jalandoni et al., 2018;~~ Sapirstein, 2016, 2018; Sapirstein and Murray, 2017; Jalandoni et al., 2018). The monitoring of active geological processes is a preventive action in risk mitigation (Stöcker et al., 2017; Turner et al., 2017b~~Deng et al. 2019~~; Diefenbach et al., 2018~~;~~, Rosa et al., 2018; Deng et al. 2019~~; Stöcker et al., 2017; Turner et al., 2017b~~). Disasters occur when two factors - hazard and vulnerability - coincide. The risk is proportional to the magnitude of the hazards and the vulnerability of the affected population. Among the deformation monitoring systems, the

50   photogrammetry technique from Unmanned Aerial Vehicles (UAVs) is spreading thanks to the high efficiency in data acquisition, the low cost compared to traditional techniques and ~~in~~ the acquisition of high resolution images (~~Fonstad et al., 2013;~~ Harwin and Lucieer, 2012; James and Robson, 2012; Westoby et al., 2012; Fonstad et al., 2013; Javernick et al., 2013; Johnson et al., 2014; James et al., 2017/a/b; James et al., 2020~~; Javernick et al., 2013; Johnson et al., 2014; Westoby et al., 2012~~). This technique is important to study the catastrophic natural events such as floods, earthquakes, landslides,

55   subsidence, etc. Different acquisition methods and the ability to obtain high ~~spatial~~spatial (centimetre) and temporal resolution (hours or days)~~s~~ (Boccardo et al. 2015) allow to acquire detailed information on the evolution of the landscape, therefore UAVs are an effective and complementary tool for field investigations. Furthermore, UAVs have other advantages including: (i) the ability to fly at low altitudes, (ii) the ability to reach remote locations, (iii) the ability to host multiple sensors (cameras, Lidar, thermal imaging cameras, navigation / inertial sensors, etc.), (iv) the ability to capture images at

60   different angles, and (v) the flexibility to carry out monitoring operations on a small, medium and large scale (Jordan et al. 2017). Ground Control Points (GCPs) are used to improve the accuracy of the resulting data. Therefore, recognisable points on the UAV imagery are measured with a high-precision surveying device to georeference~~d~~ the data. In this process a correct number of GCPs is required which lead to a greater accuracy of the resulting data (point clouds, 3D grid, orthomosaic or Digital Surface Model (DSM)). The precision of the resulting data is also controlled by other variables, such as: the focal

65 distance of the camera; flight path and flight altitude; the orientation of the camera; the picture quality; the processing chain and the category of UAV system (fixed or rotary wings).

In this paper, we present the results and analysis of the surface deformation monitoring of the mud volcano of Santa Barbara (Caltanissetta, central Sicily) (Fig.1). We have applied the statistical analysis of significant changes with ~~95%~~ Level of Detection $_{95\%}$ (LoD $_{95\%}$~~95%~~). In detail, we used precision maps and the M3C2-PM (Lague et al., 2013; James et al., 2017b)

70 algorithm to determine the surface variations. The statistical analysis allows to verify i) the uncertainty between the different surveys, ii) the spatial variability of the accuracy in the surveys (James et al., 2017/b), iii) the quality of the georeferencing of the surveys based on the number of GCPs.

75

Figure 1: Aerial view of the Santa Barbara mud volcano. Photo taken by the UAV from the ~~east~~west side of the mud volcano with two red scale bars derived from orthophotos.

The mud volcano of Santa Barbara is located within the Caltanissetta foredeep basin of the Apennines-Maghrebian
80 collisional chain which developed from the Late Miocene to the Quaternary, along the border of the converging Eurasia-Nubia plate (Catalano et al., 2008; Dewey et al., 1989; Serpelloni et al., 2007). This structural domain is formed by a foreland fold and ~~a~~ thrust belt involving the deposition of clastic sediments which were gradually deformed~~contracted~~ ~~and moved~~ from the late Miocene to the Pleistocene (Monaco and Tortorici, 1996; Lickorish et al., 1999, and references therein).

According to Madonia et al., (2011) mud volcanoes are most of the time in stasis, but they represent~~are~~ a preferential way for
85 rising fluids rich in methane and sludge, therefore they can be considered a risk to urbanized areas or sites with an economy dedicated to natural attractions.

On the mud volcanoes (e.g. Ayaz-Akhtarma and Khara Zira Island mud volcanoes in Indonesia), geomorphic/structural features have been observed from one year to shortly before the paroxysmal event (Antonelli et al., 2014; Madonia et al., 2011). Also the area of the Santa Barbara volcano was affected in 2008 by paroxysmal mud eruption which was preceded by

90 deformation features (Fig.2). Moreover, the surface of the mud volcanic cone is incised by a drainage system (Fig.1) characterised by hydrographic basins with elongated dendritic geometry arranged to a centrifugal development from the areas of the summit craters towards the lower slopes of the volcano complex. The higher order of the thalwegs present deep recessed meanders (landscape rejuvenation process). This morphometric structure is typical of uplifting areas and therefore relative decrease of the base level. This suggests an inflection process of the volcano ground surface induced by increase of

95 fluid pressure inside of shallower stagnation chamber which is located at a depth of about 30 m (Imposa et al., 2018). The stagnation chamber has a "sill-like" geometry, a radius of about 50 m and a thickness of about 30 m. This morphostructural configuration supported by geophysical data configures the active geological structure as a high potential geological hazard.
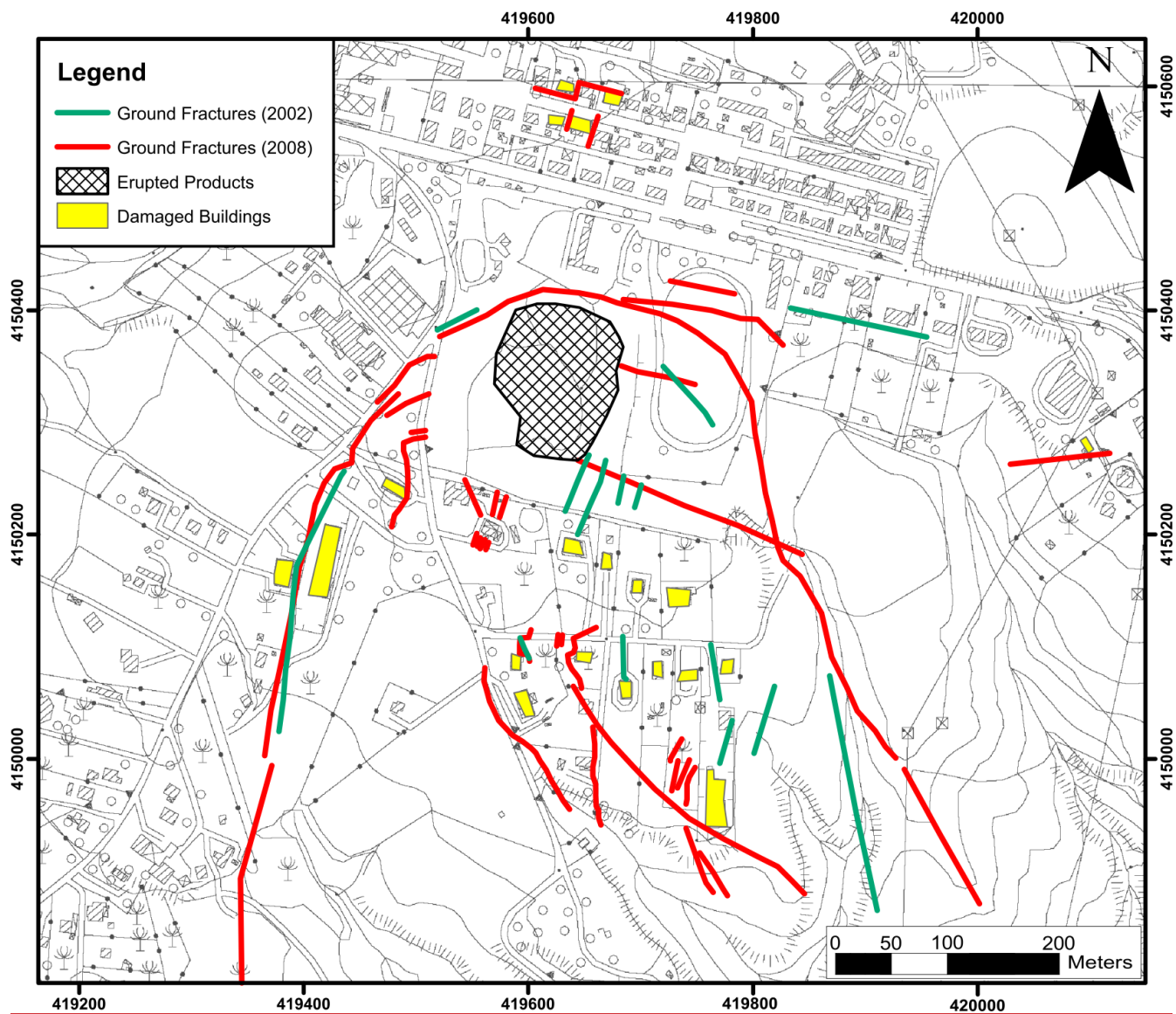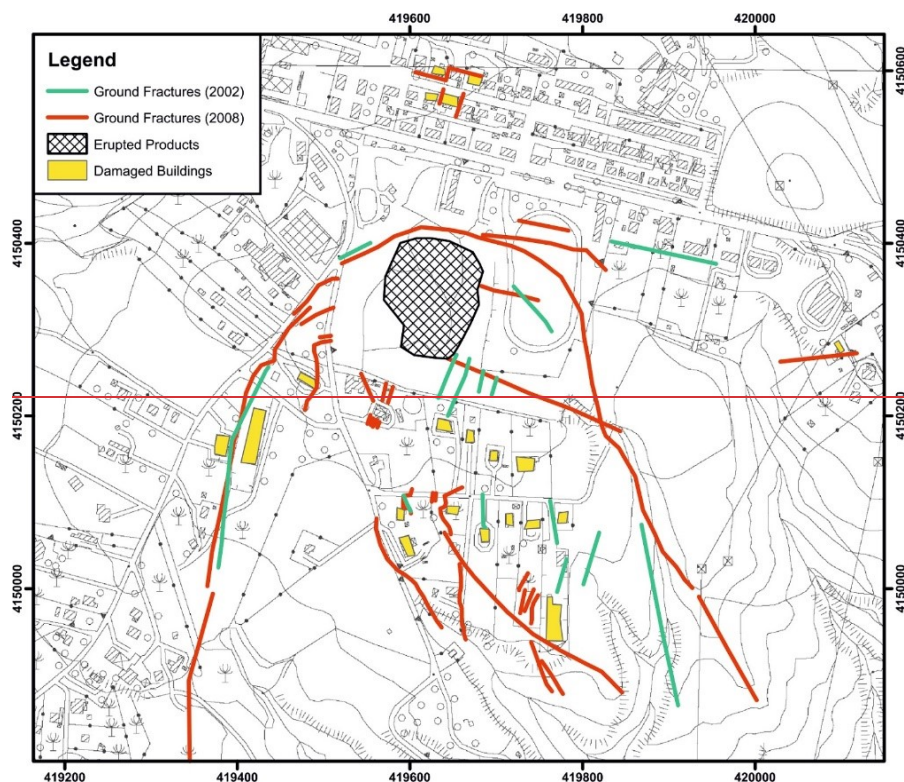
Figure 2: Cartographic extract with the location of the major fractures (in red) detected on the ground and the damaged structures (in yellow) related to the paroxysmal event of 2008. In green fractures detected in 2002. The base map is Carta Tecnica Regionale 2008 (CTR). The reference system is WGS 84 / UTM zone 33N.

On the surface, fractures and shear lineaments- extend outside the volcano the area~~s of the volcano~~, (Madonia et al., 2011; Bonini et al. 2012; INGV, 2008a; Regione Siciliana, 2008) and they highlight the high stress and strain environment induced by the mud volcano (Fig.2). Such structures have been detected on 2002 and 2008~~in the past~~ ~~and~~ we speculate that they are still active (Fig.2). This development has often been a precursor of paroxysmal events such as the 11th August 2008 event (INGV, 2008a; Regione Siciliana, 2008).

2. Methods

2.1 Local Network

In order to monitor active deformation in the mud volcano area, a local GNSS network was created according to the criteria
115 described by De Guidi et al (2017), in particular ensuring: i) ~~ensuring~~ the basic requirement of spatial and temporal stability ii) absence of possible gravitational instabilities in both static and dynamic conditions at sites and iii) a panoramic and elevated position for the Theodolite Total Station (TST).

According to these criteria two GNSS benchmarks were created: CTN0 and CTN1, located on the roof of a building on the northern sector of the studied area (Fig.3).

120
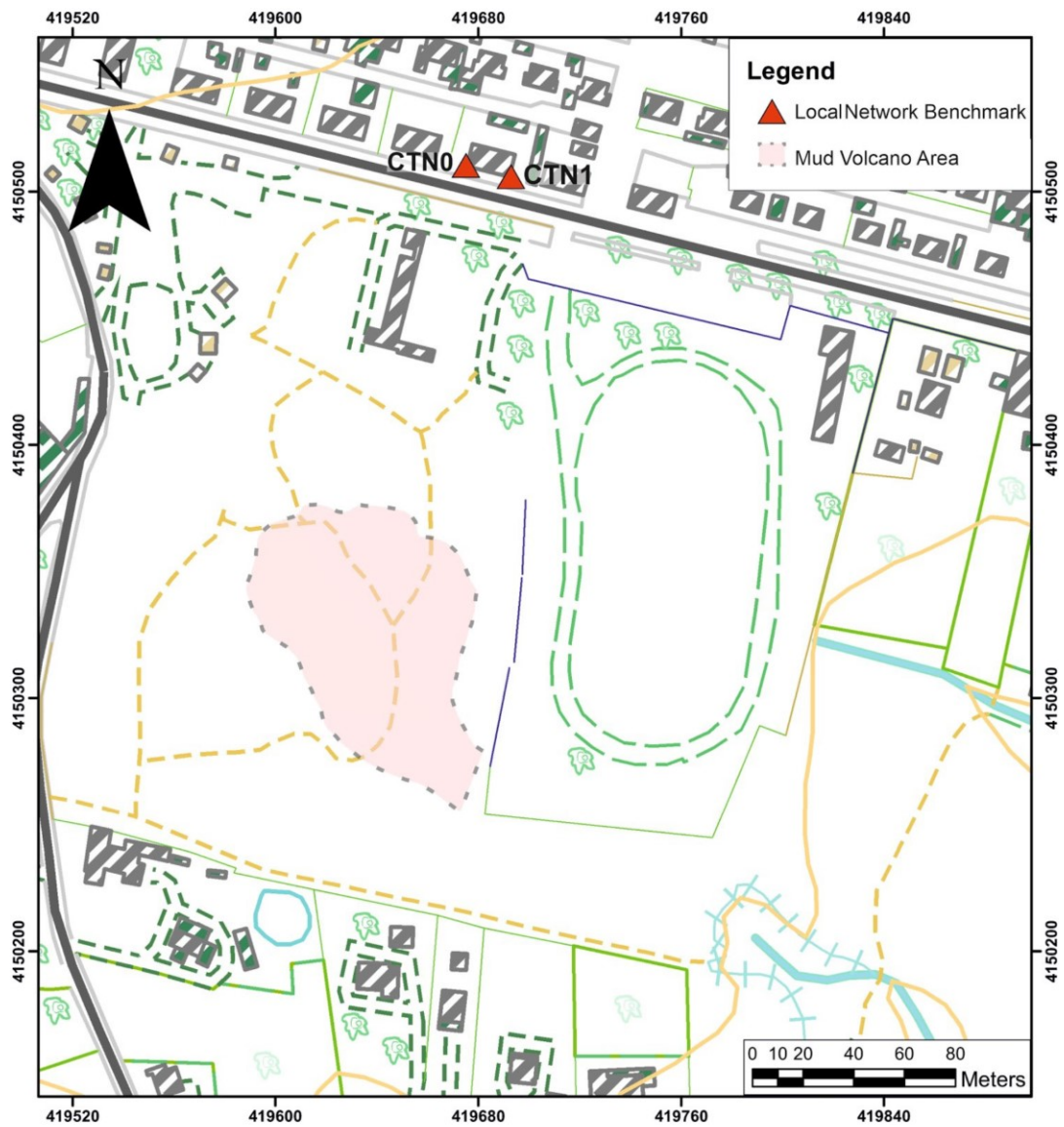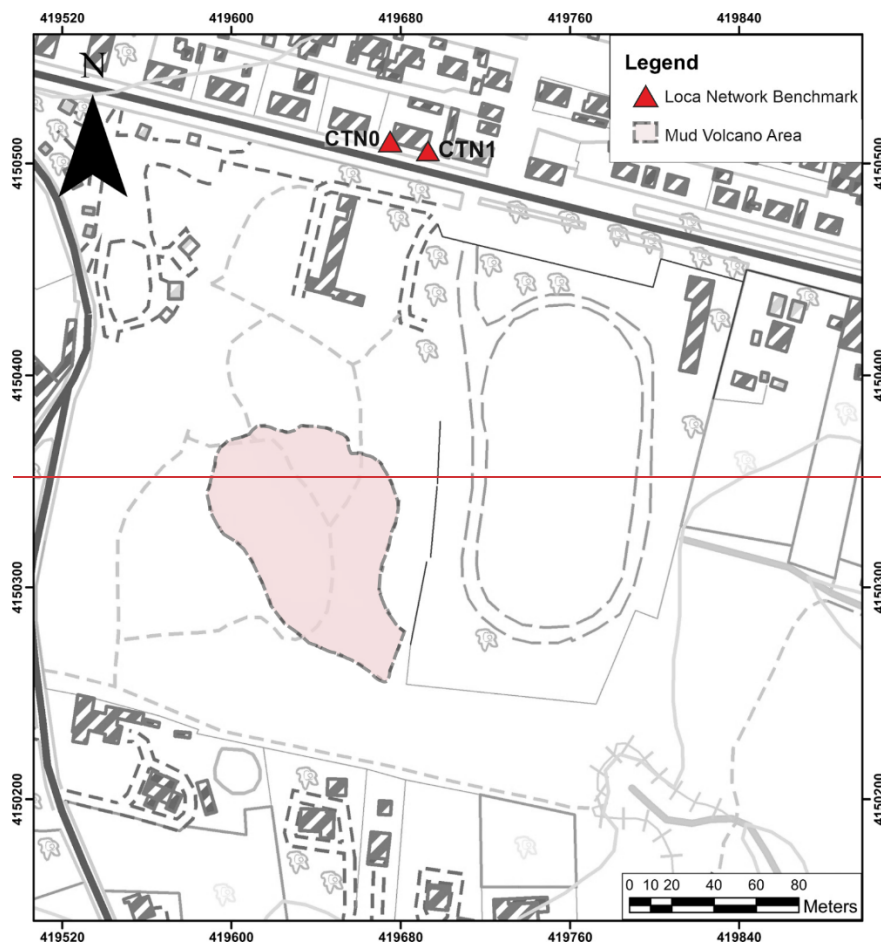
Figure 3: Chorography of the eastern periphery of the inhabited area of Caltanissetta (Santa Barbara Village). The base map is Carta Tecnica Regionale 2008 (CTR). The reference system is WGS 84 / UTM zone 33N.

125

The benchmarks were surveyed using double frequency (L1/L2) receivers (TOPCON Hiper V and HiPer SR) in static mode. Once the stability of the benchmarks has been assessed, we surveyed CTN0 and CTN1 5 and 2 times respectively.

Post processing of GNSS data was carried out by AUSPOS Online service (Geoscience Australia, 2011; Jia, M et al., 2014).

To process the CTN0 data of 2018/02/28 survey, AUSPOS used 15 IGS stations to compute the baselines: ANKR, BOR1,
130 BRUX, BUCU, GANP, GRAS, GRAZ, LROC, MAT1, MEDI, SOFI, TLSE, VILL, YEBE and ZIM2 with an average of ambiguity resolution of 90.0%, position uncertainty (95% C.L.) are respectively of 0.005 m, 0.005 m, 0.016 m for East, North and Ellipsoidal height.

To process the CTN1 data of 2018/11/26 survey, AUSPOS used 15 IGS stations to computed the baselines: ANKR, BOR1, BRUX, BUCU, GANP, GRAS, GRAZ, LROC, MAT1, MEDI, SOFI, TLSE, VILL, YEBE and ZIM2 with an average of ambiguity resolution of 84.5%, position uncertainty (95% C.L.) are respectively of 0.007 m, 0.007 m, 0.024 m for East, North and Ellipsoidal height.

Finally, the optimal ITRF2014-UTM33N coordinates have been definitively assigned to CTN0 and CTN1.

2.2 Ground Control Points (GCPs)

Various acquisition methods of Ground Control Points (GCPs) were tested in order to define the most suitable one. The main function of GCPs is to geo-reference outcomes from SfM.

Initially (2016-2018) we used only GNSS receivers in different configurations: Real Time Kinematics (RTK) and Static Ultra Rapid. The GPCPs were made of 50 cm x 50 cm alveolar polypropylene square targets. Using these configurations (Tab. 1), errors ranging from centimetre to decimetre were recorded. In these early phases, errors were only computed by SfM software PhotoScan (v 1.4.5.7554).

PhotoScan provides different types of error estimation: XY error (m) - root mean square error for horizontal coordinates for a GCP location; Z error (m) - error for elevation coordinate for a GCP location; Error X, Y and Z (m) - root mean square error for X, Y, Z coordinates for a GCP location; Error Img (pix) - root mean square error for X, Y coordinates on an image for a GCP location averaged over all the images; Total Error (m) - implies averaging over all the GCP locations.

Using Static Ultra Rapid mode, the total error was about 18 cm, whereas using the RTK configuration the total error were reduced up to about 4 cm. (Brighenti et al, 2018).

From 2018 the use of the TopCon DS-103 TST was introduced, obtaining lower values on the GCP errors than those measured with the GNSS technique (Tab.1). With this measurement technique the total error has been reduced to about 3 cm. On the first 3 campaigns, we used 6 GCPs to georeferenced the cloud points 6 GCPs (Fig.4). In the following section, these first 3 campaigns will be not considered in the computation of the significant changes for their incomparable to the last campaigns. Since 2019, we preferred to use only the TST has been used for the GCP survey and, according to Tahar et al. (2013), the number of GCPs has been increased (Tab.1). Considering these two improvement, the total error has been reduced to about 1.4 cm and in the last campaign about 0.7 cm.

DATE	METHOD OF SURVEY	GCP NUMBER	X ERROR (CM)	Y ERROR (CM)	Z ERROR (CM)	TOTAL ERROR (CM)	IMG ERROR (PIX)

2018/02/28	Static Ultra Rapid	6	12.06	8.85	10.02	18.01	0.587
2018/04/16	RTK	6	2.18	1.79	3.34	4.29	0.326
2018/04/16	TST	6	2.04	1.39	1.68	2.99	0.325
2019/07/29	TST	29	0.78	0.95	0.72	1.43	0.244
2019/09/13	TST	30	0.79	0.84	0.86	1.45	0.316
2019/10/14	TST	31	0.78	0.66	0.78	1.29	0.311
2020/01/13	TST	31	0.95	0.82	0.77	1.48	0.237
2020/06/15	TST	26	0.43	0.39	0.45	0.73	0.249

160   **Table 1: Average RMSE of GCPs obtained for each survey and for each technique used to determinate the GCPs coordinates: X (Easting), Y (Northing), Z (Altitude) and the Total Error. The image residual (IMG ERROR, in the table) is shown.**

Count	X error (cm)	Y error (cm)	Z error (cm)	XY error (cm)	Total (cm)
6	8.84501	6.28639	9.78311	10.8514	14.6103

Count	X error (cm)	Y error (cm)	Z error (cm)	XY error (cm)	Total (cm)
30	0.793059	0.848473	0.868639	1.1614	1.4503
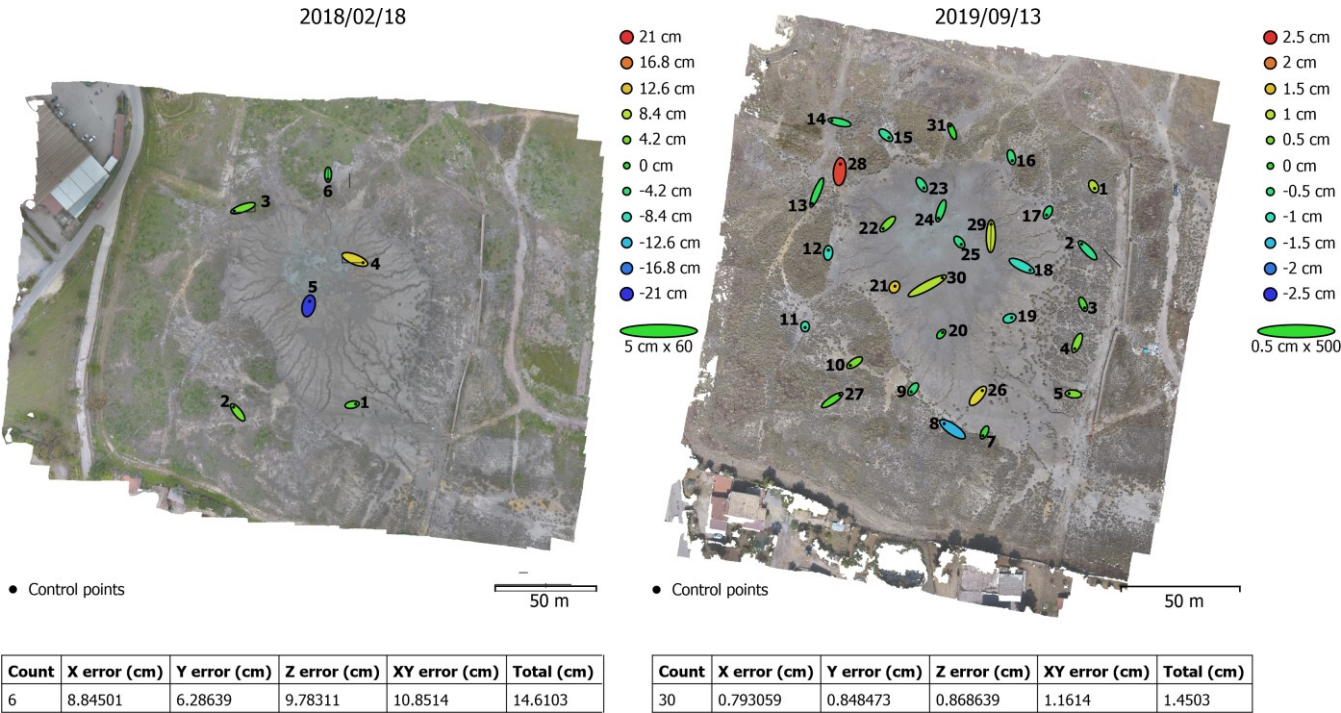
Figure 4: GCPs locations and error estimates. Z error is represented by the colour of the ellipse. X, Y errors are represented by
165   **ellipse shape. GCP locations are marked with a dot. Note that the different scale of the error ellipse in green: in the left image the**

ellipse in X direction is enlarged 60 times, in the right image it is enlarged 500 times. The reference system is WGS 84 / UTM zone 33N.

In the last two campaigns we used ~~Theodolite Total Station (~~TST~~)~~ to obtain the coordinates of the GCPs. The TST was positioned on the CTN0 point of the local network~~,~~ (Fig.3) which coincides with the roof of the nearby private houses in the northern part (Fig.5-A). A classic celerimetric survey was carried out.

The measurements of the GCPs were carried out with a surveying ranging rod equipped with a reflecting prism (offset of -30 mm) assisted by a tripod with a ~~spirit~~ ~~bubble~~ level (Fig.5–B), to ensure the ~~upright~~~~verticality~~ and stability of the measurement.

Figure 5: A) TST DS 103 placed on the fixed metal base in coincidence with point CTN0. B) Surveying ranging rod on the mud volcano during the survey phase.

~~Based on the CTN0 point and directing on the CTN1 point, we~~ We assumed a "Marker Accuracy" on PhotoScan ~~an instrumental error~~ of 5 mm due to the instrumental error ~~(named in PhotoScan "Marker Accuracy")~~. This value has been

assumed due to the uncertainty of the CTN0 and CTN1 point coordinates, obtained through GNSS measurements, considering that the uncertainty derived from the TST is negligible.

To validate GCPs data we ~~have done~~performed an analysis ~~(compared with the SfM software data)~~ using the python script "Monte_Carlo_BA.py", with a statistical iterative approach (Monte Carlo approach) (James et al. 2017/a). For clarity, the following terminology will be used in the text:

- GCPs are the points measured in the field. They can be used as control points or check points within the bundle adjustment (James et al. 2017/a).
- Control points are GCPs when they are tied to the model ~~during~~ in the bundle adjustment.
- Check points are GCPs when they are not tied to the model in the bundle adjustment.

This script modifies the percentage of GCPs which are used as check points or control points and applies to the check points random variations (James et al. 2017/a). To be more precise values ranging from 10% up to 80% of GCPs have been set.

2.3 Photo Acquisition

We have performed five measurement campaigns in approximately one year. The same flight plan was used for all five of them. The AOI (Area Of Interest) was captured by a DJI Phantom 4 Standard, a quadcopter UAV, at a flight height of 33 m above the ground. The sensor size of the UAV's digital camera is 6.17 mm by 4.55 mm, capable of shooting images with a resolution of 12 MP (4000 × 3000 pixels) with a mechanical shutter. Each flight planning was carried out with the Pix4D Mapper software, adopting a frontal and side overlapping of 80% and 70% respectively. The camera was set-up in a nadir~~al~~ orientation to capture vertical imagery. The flight was carried out in a single grid (simple geometric flight patterns without intersections). An average of 280 images for each survey were acquired with about 1.1 cm Ground Sampling Distance (GSD).

2.4 Data processing through Structure from Motion (SfM) techniques ~~Data Processing SfM~~

The photogrammetric processing was performed using the commercial software Agisoft PhotoScan. The photogrammetric processing is based on the workflow formulated by the USGS (2017). ~~with~~ Steps of the processing chain regarding Tie Point Accuracy and Marker Accuracy have been performed according to James et al. (2017) (Fig.6) ~~steps of the processing chain of Tie Point Accuracy and Marker Accuracy recommended in James et al. (2017) (Fig.6)~~.

ha

Step 1

Photo Setup, Alignment, Initial Adjustment

Add Photos
⇩
Set Coordinate/Projection
⇩
Camera Calibration
⇩
Align Photos
⇩
Initial Bundle Adjustment
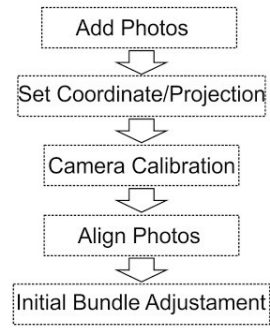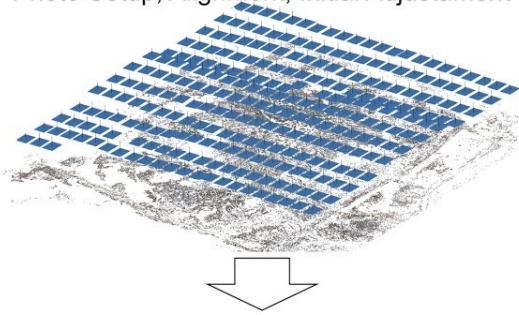
Step 2

Error Reduction & Bundle Adjustment

Reconstruction Uncertain ← Repeat Until Set Level 10
⇩ Bundle Adjustment
Projection Accuracy ← Repeat Until Set Level 2-3
⇩ Bundle Adjustment
Tighten Tie Point Accuracy Value
⇩ Bundle Adjustment
Add Control Points (Markers)
⇩ Bundle Adjustment
Reprojection Error ← Repeat Until Set Level 0.3
⇩ Bundle Adjustment
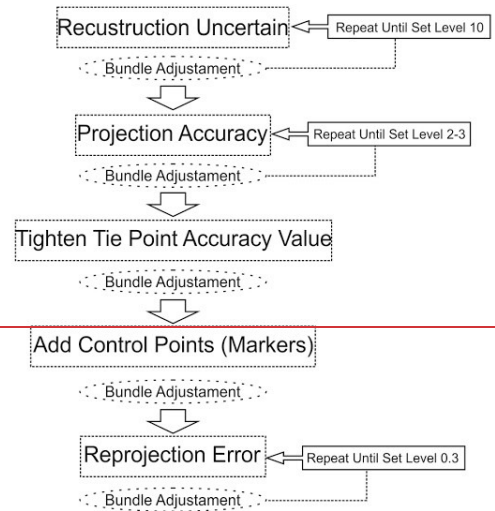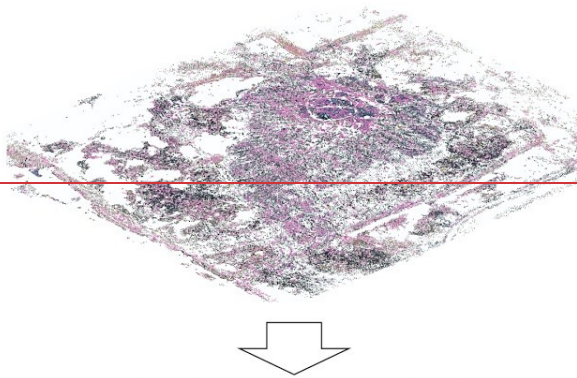
Step 3

Build Dense Point Cloud, Mesh, Texuture, DSM, Orthomosaic

Build Dense Point Cloud
⇩
Build DSM
Build Orthomosaic
Build Mesh
Build Texture
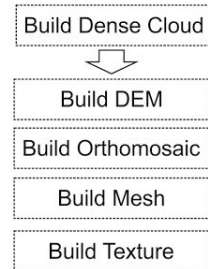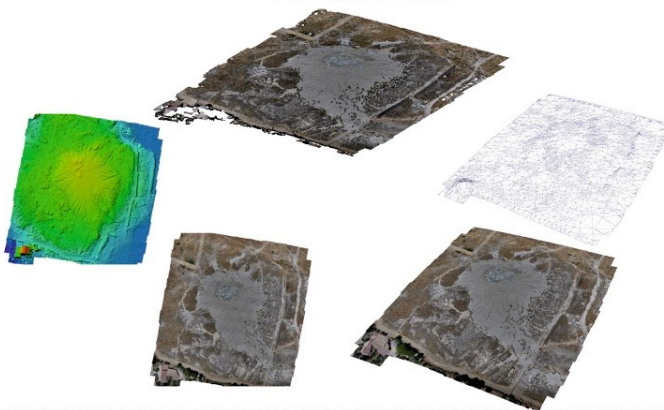
Figure 6: Simplified block diagram of the photogrammetric processing chain.

240 The procedure above is conventional, but we modified someame parameters during the cleaning procedure of the sparse point cloud. We adopted the optimal values defined on the workflow (Fig. 6) of "Reconstruction Uncertain" and "Projection Accuracy" in the "Gradual Selection" option in PhotoScan. Finally, after that the model has been georeferenced, we adopted the optimal value of the "Reprojection Error" (Fig. 6) (USGS, 2017).

The first parameter, "Reconstruction Uncertain", improves the geometric reconstruction of the cloud point.

245 The second one, the "Projection Accuracy", improves pixel mismatches in images.

After these operations, the GCPs can be tied to the sparse point cloud.

After the georeferencing procedure, we have to perform the "Gradual Selection" option, adjusting the "Reprojection Error" values to reduce the Residual Pixel Errors.

Furthermore, appropriate pixel values of tie point accuracy and marker accuracy are set, following the suggestions of James, 250 et al. (2017-/-b).

After that, we applied the "precision_estimate.py" script (James, et al. 2017-/-b). The script operates, by an interactive Monte Carlo approach, to estimate the accuracy of SfM surveys through photogrammetric and georeferencing parameters, which are then used to provide spatially variable confidence limits for the detection of surface variations.

The precision estimates are calculated through multiple "bundle adjustments" ("Optimize Camera Alignment" in PhotoScan) 255 with different pseudo-random offsets (in this case 4000 pseudo-random offsets) (Fig.7), applied to each image and checkpoint. The pseudo-random offsets are derived from normal distributions with standard deviations representative of the appropriate accuracy within the survey (James et al. 2017-/-b).
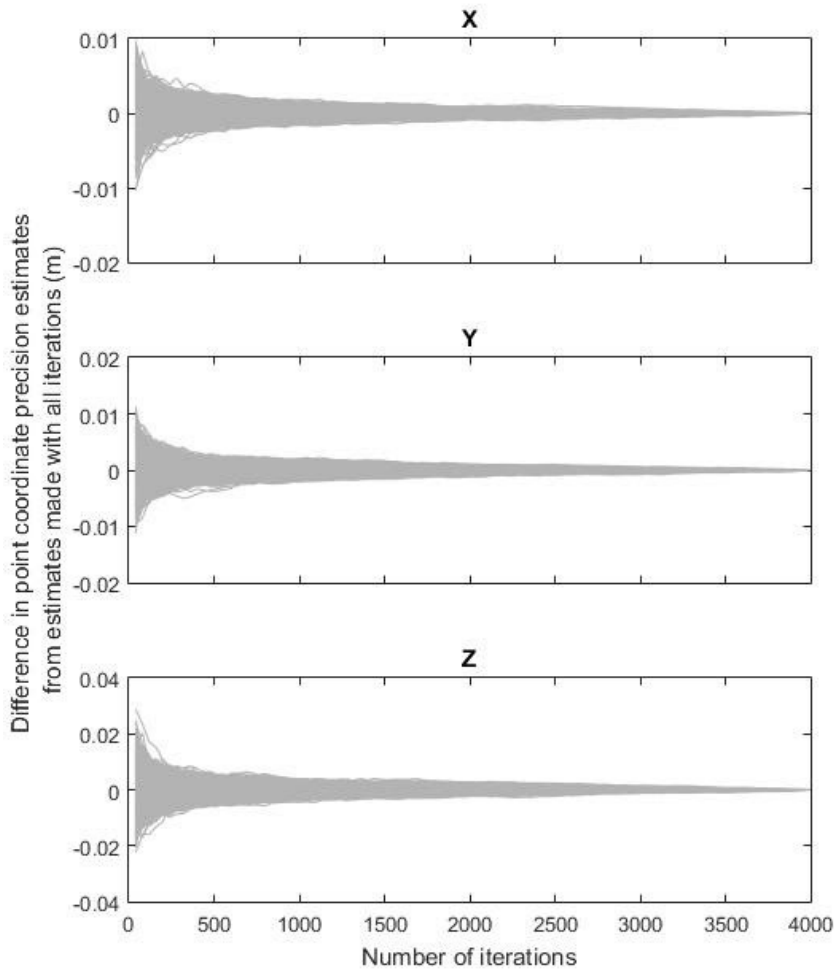
After that, the Sfm-Georef software (James and Robson, 2012) reads the output given by the Monte Carlo python script, setting to each point of the sparse cloud different values of precision on the three spatial components. The results of the script, read by Sfm-Georef, are estimates of the error of the individual points of the sparse cloud point in the three different spatial dimensions (Fig.8).
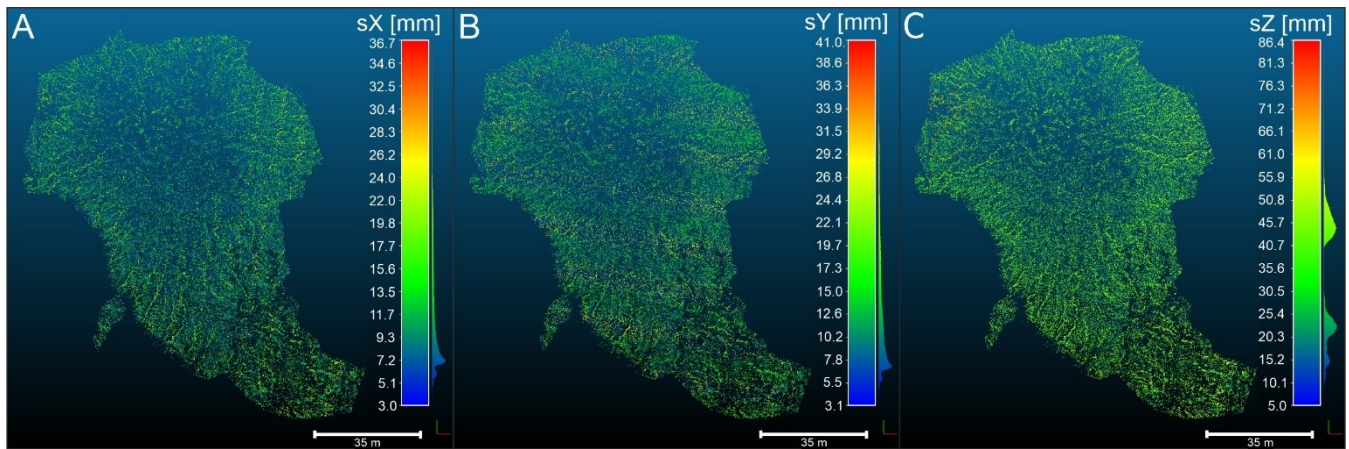
Figure 8: 3D error estimates of each point of the sparse cloud of the 19/09/13 survey. The error (sX, sY, sZ) is in mm. A) and B) The horizontal errors (X and Y component) are shown. C) The vertical errors (Z component) are shown. The reference system is WGS 84 / UTM zone 33N.

The 3D topographic change is usually detected from ~~sparse cloud points~~ sparse_point_clouds that have been cleaned to exclude the vegetation that interferes with the comparison techniques. Next step is to link those points to the precision estimates of the sparse cloud; this has been done in CloudCompare v. 2.11.

Through CloudCompare the sparse cloud is interpolated (with the relative precision values on the three-dimensional components) with the ~~dense cloud point~~dense point cloud. In this phase we decide which interpolation technique is the mo~~st~~re suitable, in this case the best is "nearest neighbors" that consider the three closest points to the sparse cloud, using the median value (better outliner mitigation) to assign the error values to the ~~dense cloud point~~dense point clouds (Fig.9). This methodology has been chosen due to the heterogeneous distribution of the points in the sparse cloud, avoiding point with null values.
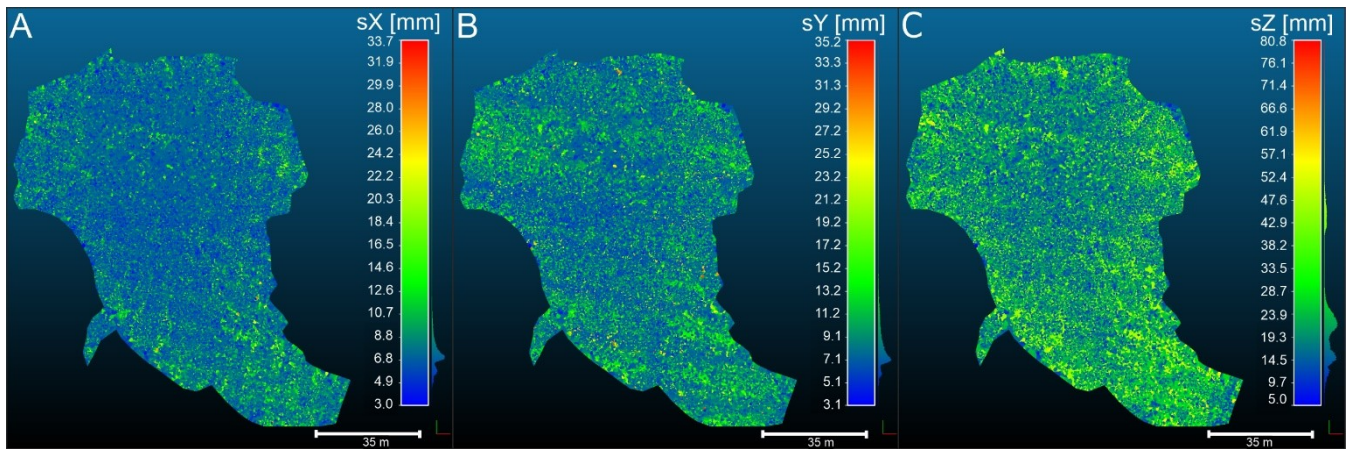
Figure 9: Estimates of the 3D error of the ~~dense cloud point~~dense point clouds obtained by interpolation with the sparse cloud of the 19/09/13 survey. The error (sX, sY, Sz) is in mm. A) and B) The horizontal errors (X and Y component) are shown. C) The vertical errors (Z component) are shown. The reference system is WGS 84 / UTM zone 33N.

Once that the precise ~~dense cloud point~~dense point clouds and their error have been obtained, it is possible to compare the surveys in order to get the changes between them. Comparisons between the surveys were performed on CloudCompare by the M3C2-PM plugin (James et al., 2017/b~~B~~; Lague et al., 2013) that identifies a statistically significant change where the topographical differences exceed a value of spatially variable uncertainty. According to James et al. (2017~~-/-~~b), the M3C2-PM is particularly suited for point clouds derived from SfM. The M3C2-PM (James et al., 2017~~-/-~~b) uses estimates of precision of the coordinates of points (3D precision map) that we have previously calculated.

The outputs of M3C2-PM are scalar values applied to the cloud:

- significant change (Fig.10-A).
- M3C2 distance (Fig.10-B).
- distance uncertainty (Fig.10-C).

The first output (Fig.10–A) shows the changes which exceed~~s~~ the uncertainty values in both point clouds. It represents a confidence interval constrained by values of Level of Detection $_{95\%}$ (LoD$_{95\%}$) which are spatially variable. This is applicable in any morphological setting, providing a reliable 3D analysis of topographical change.

The second output (Fig.10-B) shows the calculated distances between the two clouds.

The third output (Fig.10-C) shows the uncertainty values of the distances and their spatial variation between the two clouds. Once the uncertainty value is defined, the changes are significant when they overtake the value of the uncertainty.
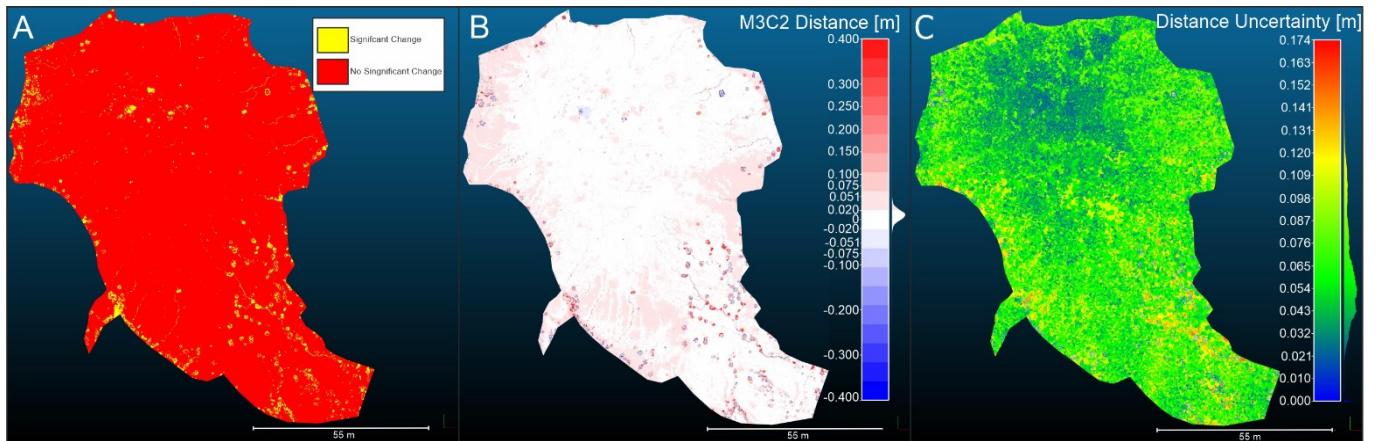
305 **Figure 10: Point clouds resulting from M3C2-PM processing, comparison between 2019/07/29 and 2020/06/15; (A) significant changes between the two point clouds with LOD%95; (B) distances between the two point clouds; (C) uncertainty of the distance between the two point clouds. The reference system is WGS 84 / UTM zone 33N.**

In the 2020/06/15 survey, we used callipers to test and validate the method of the measurements. Five numbered callipers,
310 with steps of increasing height of about 2 cm, were positioned on the mud dome. The heights are 2, 4, 6, 8 and 10 cm.

These were used to obtain an instrumental sensitivity of the measures (Fig.11). All callipers are detected, we show as example the smallest (Fig.11).
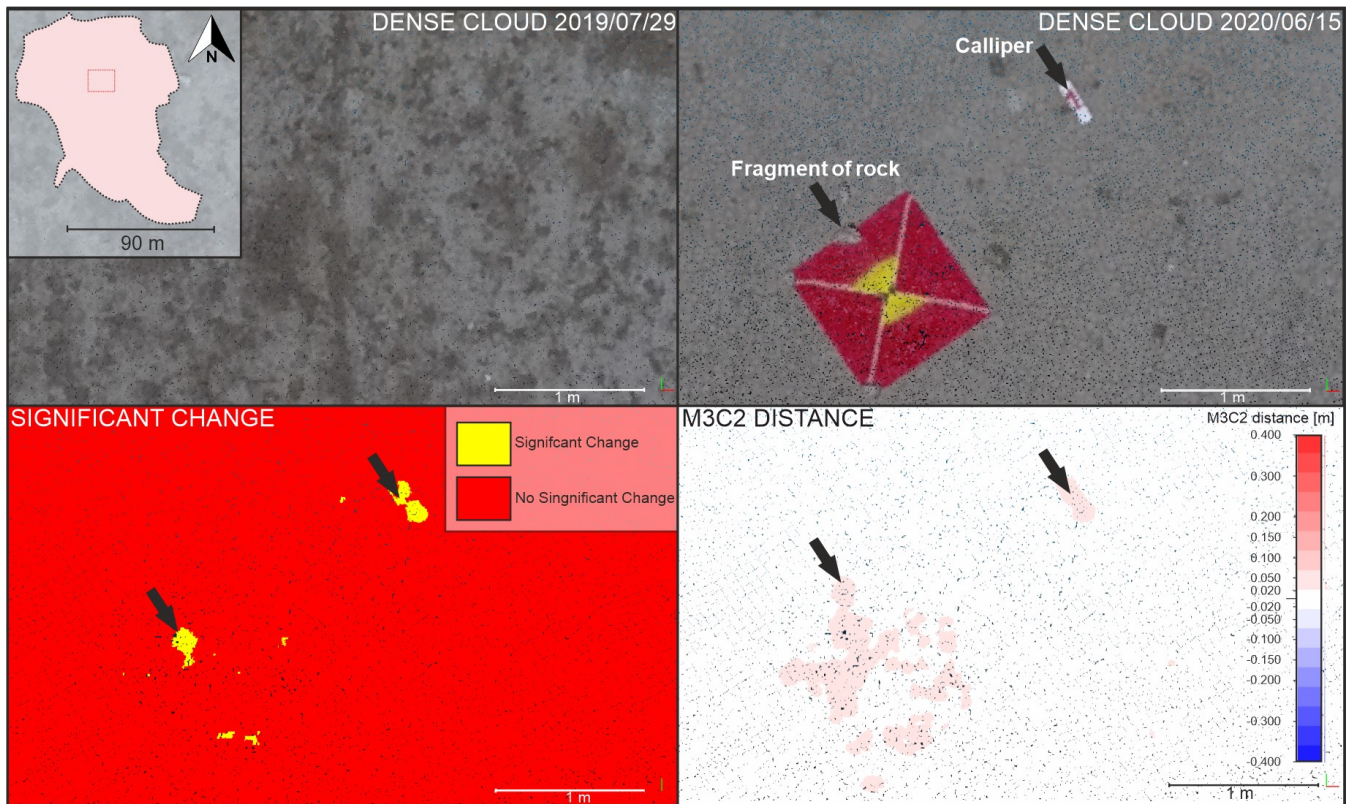
Figure 11: On the upper part of the figure the dense point cloud of the two surveys of the same area carried out on 2019/07/29 (left) and 2020/06/15 (right) are shown. On the lower part the clouds with the significant change (left) and the M3C2 distance (right). The arrows indicate the significant changes between the surveys. The calculated changes between the two clouds estimate an altitude increase of about 6.3 cm for the fragment of rock used to maintain the target in position and an increase in height of about 2.5 cm for the calliper which is 2 cm thick. The reference system is WGS 84 / UTM zone 33N.

3. Results

As illustrated in section 2.2, the results show that using between 40 and 60 % of the GCPs (as control points) the RMSE value has minimal variation. ~~As illustrate on the section 2.2, the results show that using a percentage of GCPs (considered as control points) between 40 and 60, the RMSE value has a slight minimal variation.~~ Thus, the optimal minimum number of GPCs is between 12 and 18. When the threshold of 60% is exceeded, ~~Exceeded the threshold of 60%~~ there are no significant improvements (Fig.12). This result has been confirmed in all campaigns.
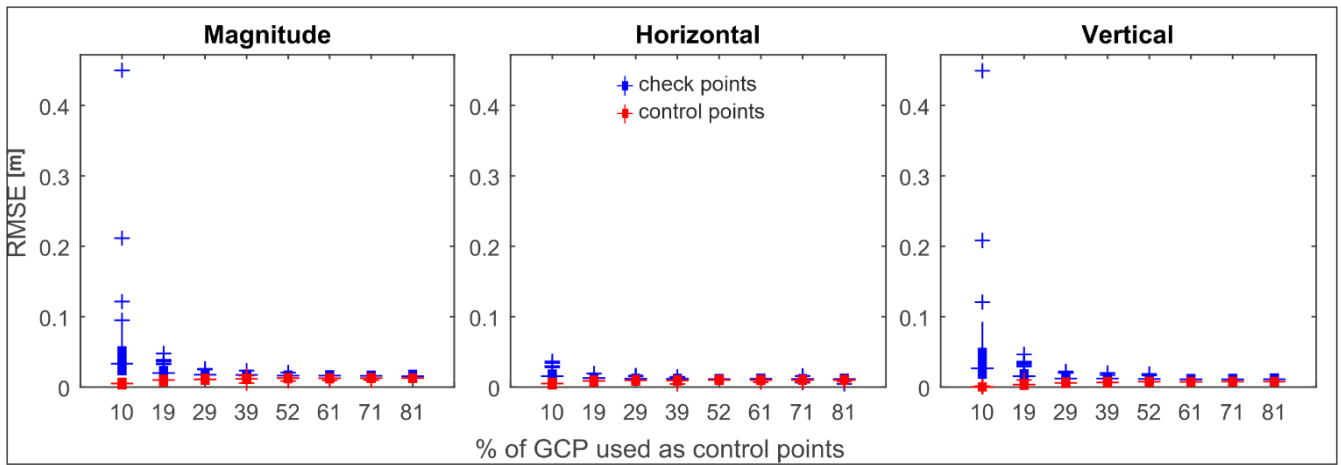
Figure 12: The boxes represent the distribution of the RMSE of GCPs (2019/09/13 survey) on the three components: Magnitude (3D), Horizontal and Vertical according to the % of the GCP used as control points. RMSE is calculated on 50 self-calibrating bundle adjustments for each % of GCPs used as control points. The GCPs are randomly selected for each self-calibrating bundle adjustments. The central bars indicate the median RMSE values, which are included in the boxes that extend from 25th to 75th percentile and the outliers are indicated by the + symbols.

The results obtained from the photogrammetric comparisons supported by geodetic topographic survey, have an average uncertainty of about 6.4 cm, with a minimum of about 2 cm and a maximum of about 12 cm, relative to an area of 42700 m² (Fig.13-A). The uncertainty of the central area has an average value of about 3.9 cm, with a minimum of about 2 cm and maximum of 10 cm, on an extension of 360 m² (Fig.13-B).
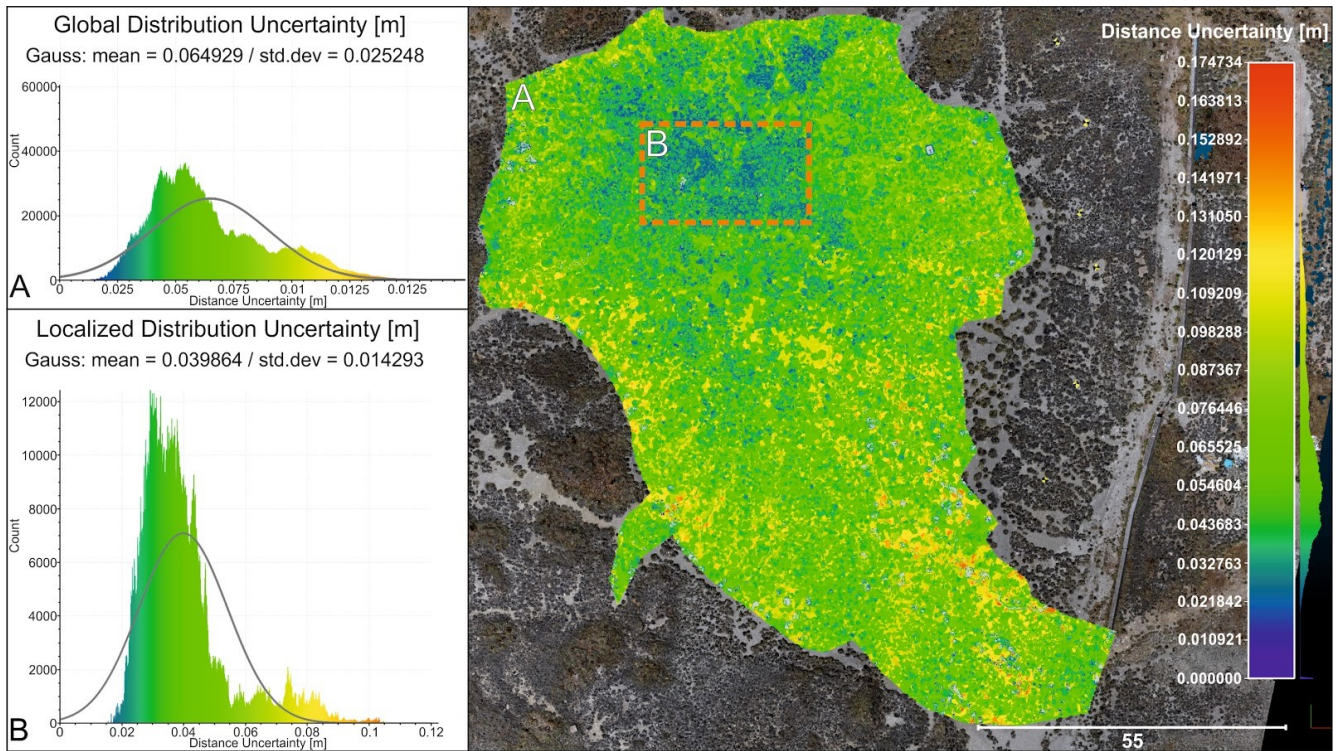
Figure 13: Points Cloud with uncertainty distance values between 2019/07/29 and 2020/06/15 (right). On the left, (A) the Gaussian distribution of the distance uncertainty over the whole area is shown, the mean is about 6.4 cm and the standard deviation is about 2.5 cm. (B) the Gaussian distribution of the distance uncertainty of the central emission area is shown, the mean is about 3.9 cm and the standard deviation is about 1.4 cm. The reference system is WGS 84 / UTM zone 33N.

During the monitoring period, in addition to natural changes, we recorded anthropogenic action, due to the relocation of objects (garbage) in the area after unauthorized access. These changes have a decimetric order of magnitude and are easily detected by the technique used (Fig.14).
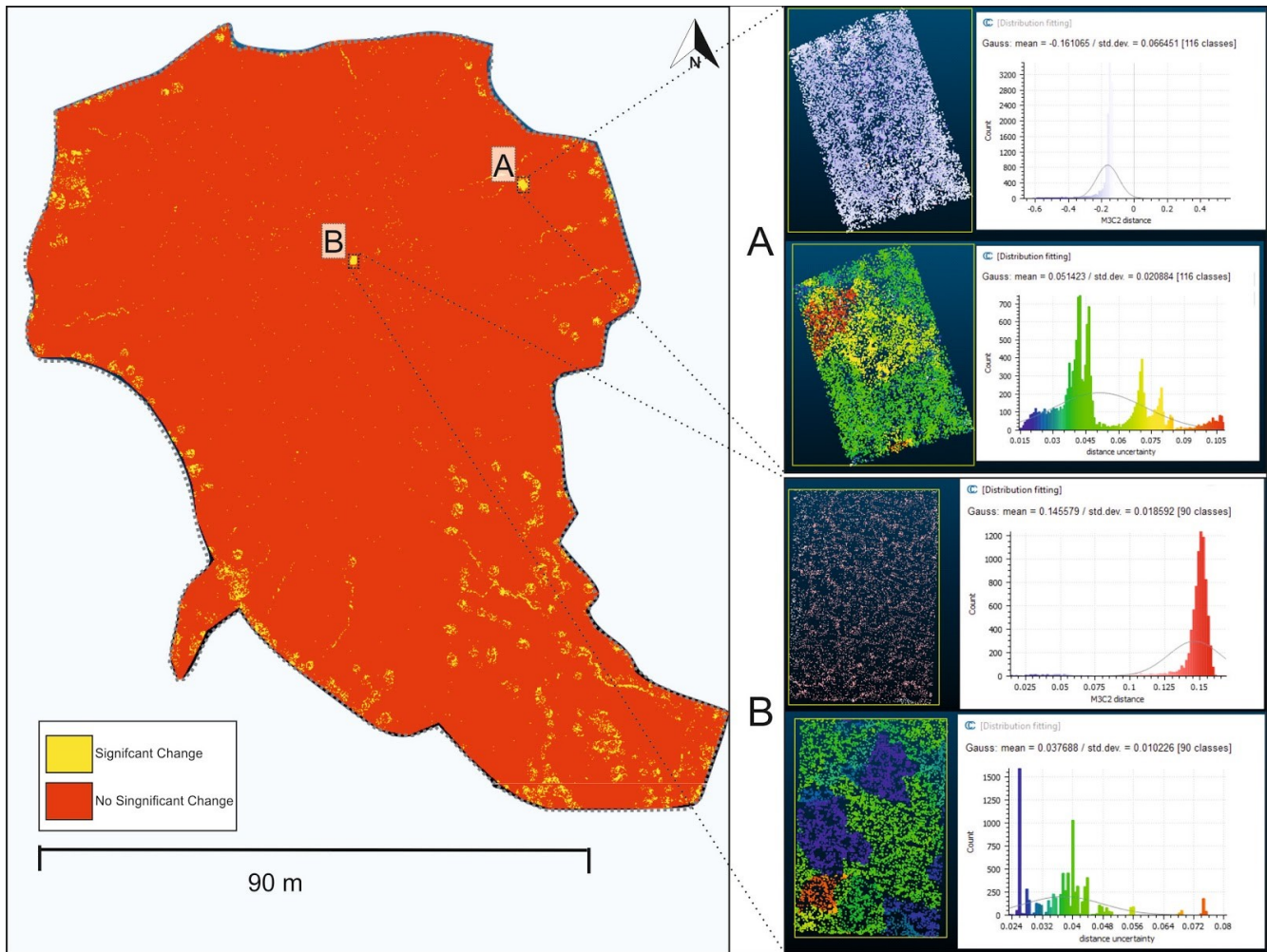
Figure 14: Enlargement of the comparison between the point clouds of the 2019/09/13 and 2019/10/14 campaigns with significant change. Two significant changes (A and B) are shown, which highlight an anthropogenic action, i.e. the movement of a wooden platform about 15 cm high. (A, upper part) a lowering of an average height of 16 cm is detected, the Gaussian distribution of the M3C2-PM distances with the mean and the standard deviation are shown. (A, lower part) the Distance Uncertain varies spatially with an average value of about 5 cm, the Gaussian distribution of the M3C2-PM distances with the mean and the standard deviation are shown. (B, upper part) an increase of height of 14 cm is recorded, the Gaussian distribution of the M3C2-PM distances with the mean and the standard deviation are shown. (B, lower part) the distance uncertain has an average value of about 3 cm, the Gaussian distribution of the M3C2-PM distances with the mean and the standard deviation are shown. The reference system is WGS 84 / UTM zone 33N.

Two types of analysis were carried out: semi-quantitative and quantitative. The surveys 2019/07/29 and 2020/06/15 (time interval of about 1 year) were chosen to perform the semi-quantitative analysis. This analysis was carried out on the whole mud volcano area ~~on the whole of the mud volcano area~~, the objective is to detect important deformations (in the order of decimetres). In order to visualize important deformations ~~To visualized important deformation~~ (Fig.15), the values of M3C2

distance ranged between -2 and 2 cm were excluded, according to the minimum value of distance uncertainty. This range was verified instrumentally with the use of callipers.

365
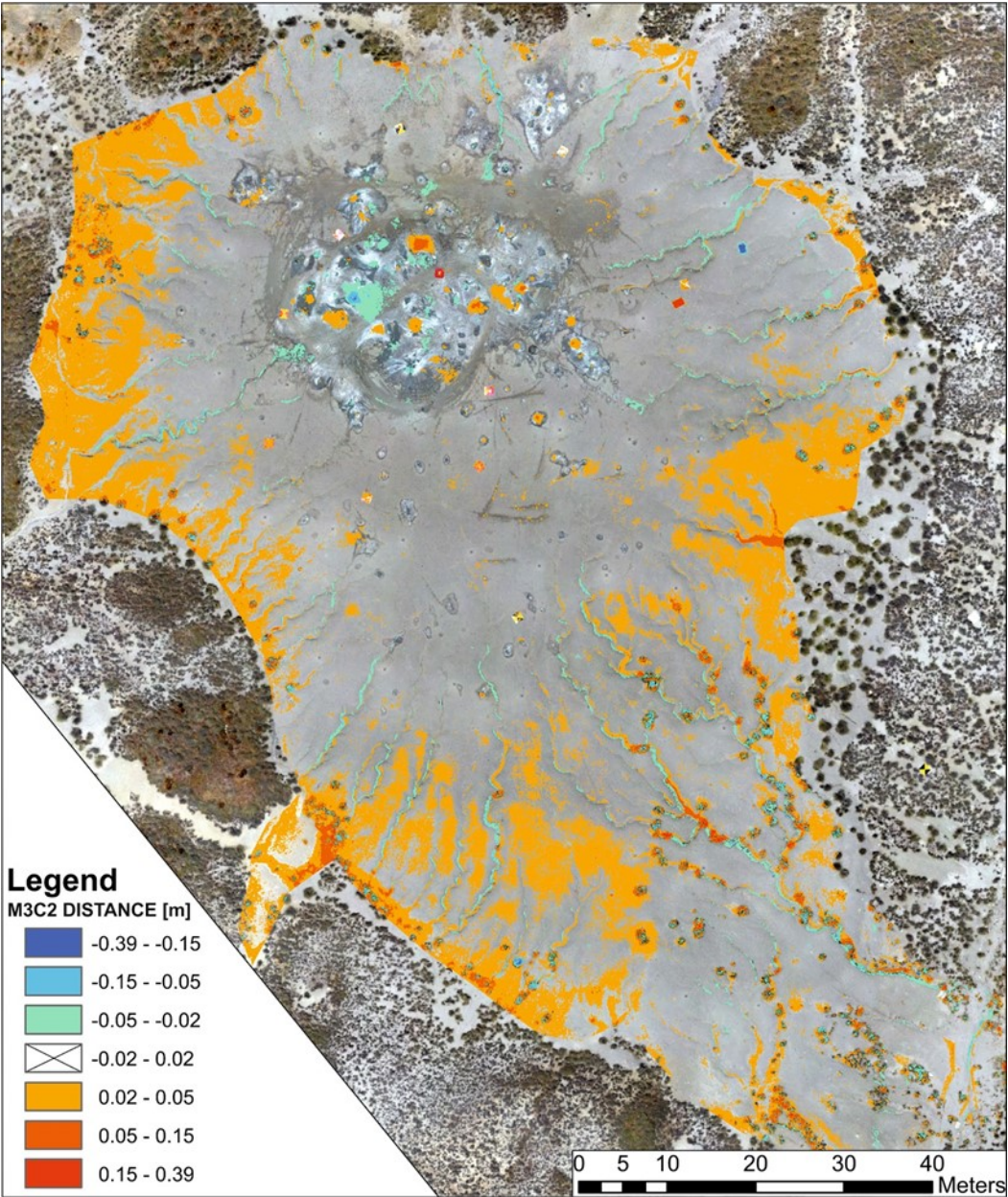
Figure 15: Orthophoto with M3C2 Distance. The distance scale has been adjusted to exclude values between -2 and +2 cm. The positive distances, observed at the margin of the mud dome, are interpreted as mud flow or sediment deposition coming from peripheral griffon vents eruptions or erosion of summit area. The reference system is WGS 84 / UTM zone 33N.

370

Considering the 2019/07/29 and 2020/06/15 surveys (Fig. 15) we observe that the total surface of the volcanic cone can be considered not affected by deformations. Only morphological changes in the volcanic structures can be underlined, such as small eruptive cones, griphons, sauces and mud pools.

The quantitative analysis was performed on small central portions of the mud volcano. The aim of the quantitative analysis is to estimate the trend and evolution of the deformation. To assess the deformation and the local morpho-structural evolution, two temporal series have been developed in two areas: Z1 (collapse zone) and Z2 (uplifting zone) (Fig.16 and Fig.17). The zones were chosen related to the significant change. On the selected zone, the average distances between points with significant change were computed by M3C2-PM. Z1 has an extension of 1 m² (Fig.16) and Z2 has an extension of 0.84 m² (Fig.17).

As master was chosen the campaign of 19/07/29 (T0) (Table 2).

T_0	2019/07/29
T_1	2019/09/13
T_2	2019/10/14
T_3	2020/01/13
T_4	2020/06/15

Table 2: Surveys used to the generation of time series.
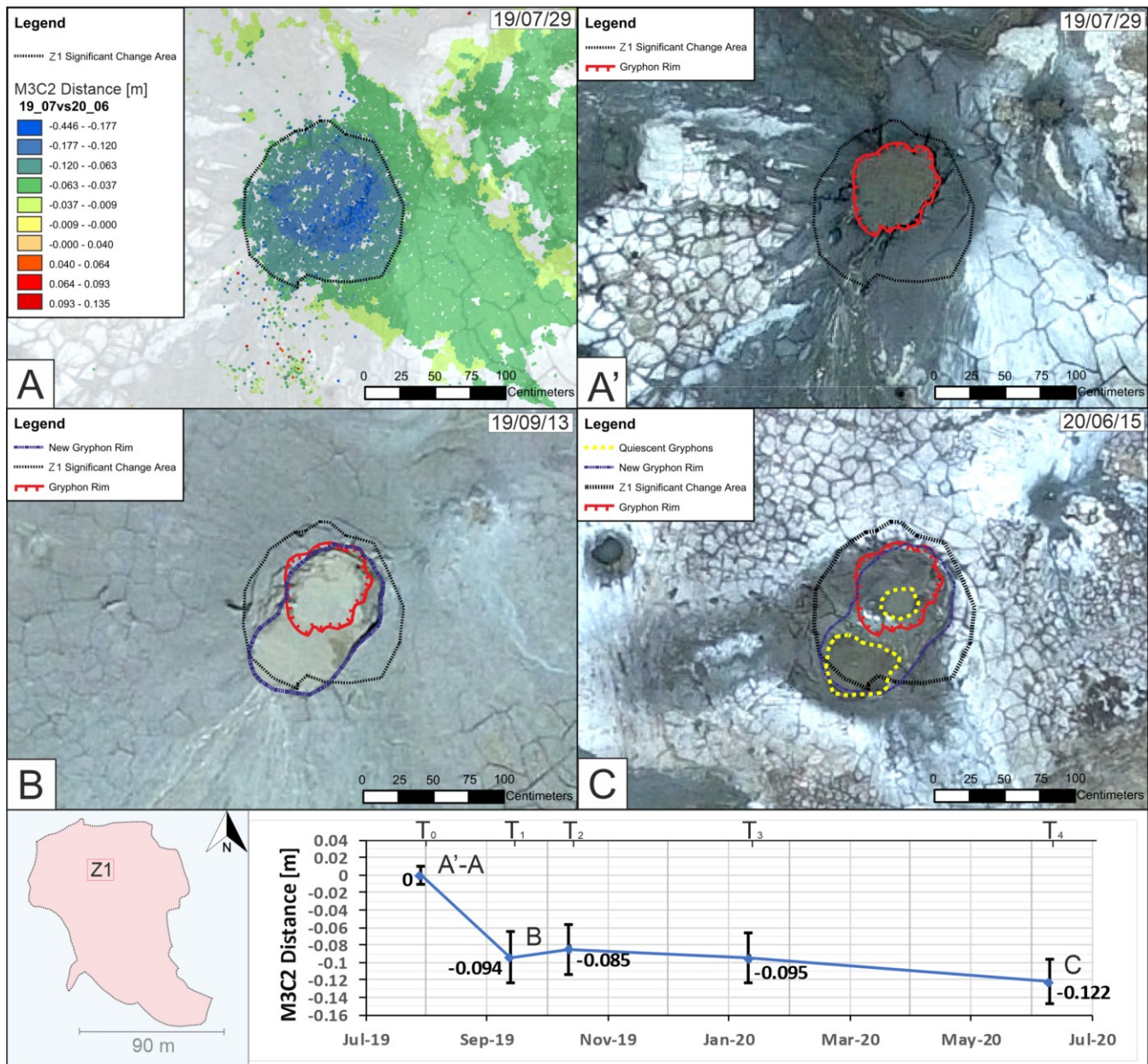
Figure 16: (A) M3C2 Distance (2019/07/29 vs 2020/06/15) of Z1; the area used to create the time series is delimited with a dashed line (selected by significant change). **(A')** Orthophoto of 2019/07/29 with the gryphon border in red. **(B)** The orthophoto of 19/09/13 highlights the expansion of the gryphon border (blue). **(C)** Orthophotos of 2020/06/15, gryphon during the quiescence phase and the split of the channel in yellow. Below the time series with a decreasing trend is shown. The reference system is WGS 84 / UTM zone 33N.

In Ffigure 16 the subsidence (about 10 cm / 60 days) of gryphon is represented by the southwest migration of the mud pool edge. In Ffigure 17, the uplift (about 4 cm / 60 days) of a blind gryphon is represented by the development of radial fractures on the cone surface. Close to the growing gryphon, another indication of deformation is the deviation of a mudslide flowing in the N-S direction towards the southern sector of the analysed area. Finally, the sudden appearance of the gryphon is well highlighted in the ortophoto of the last survey (Fig.-17).
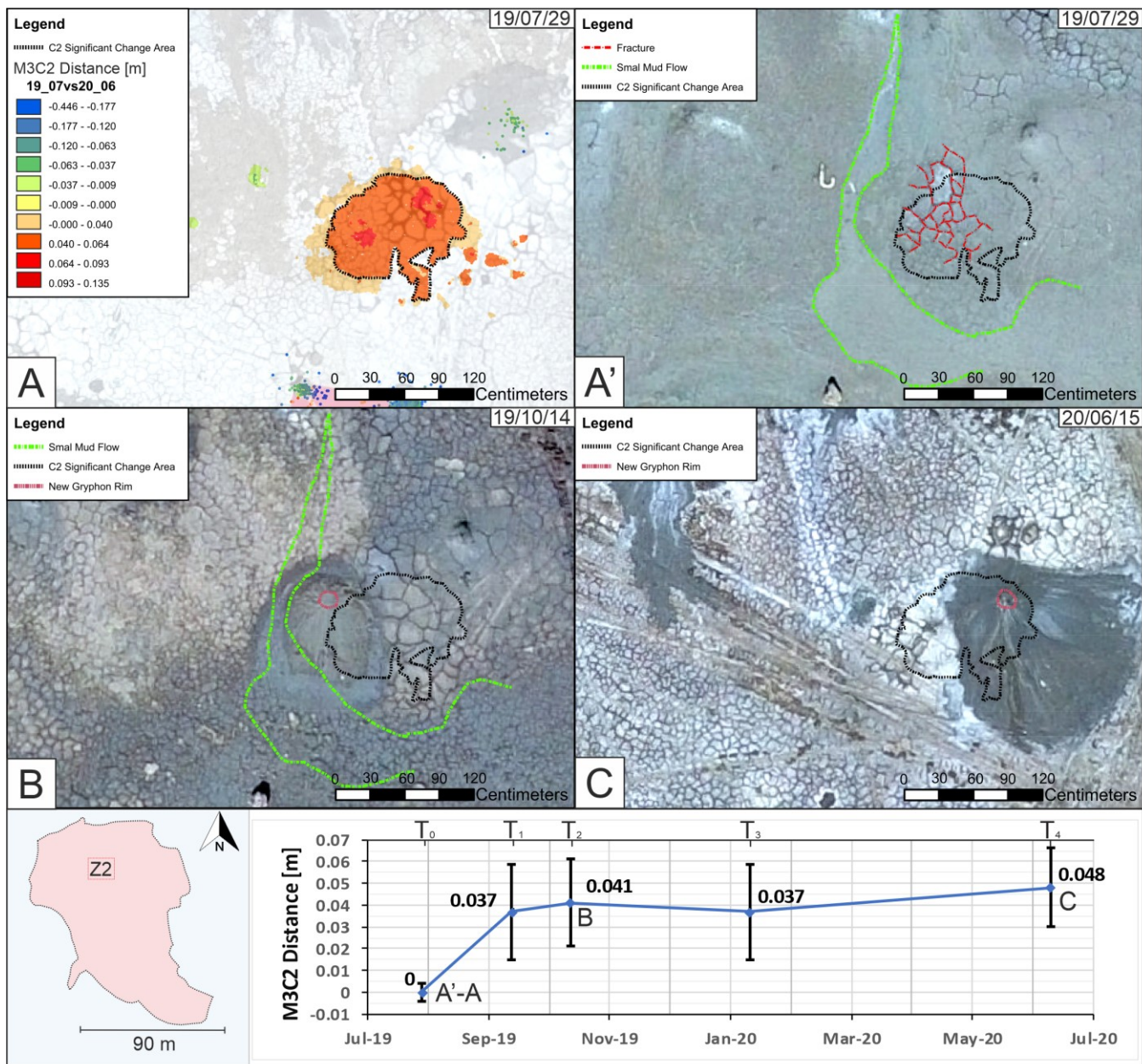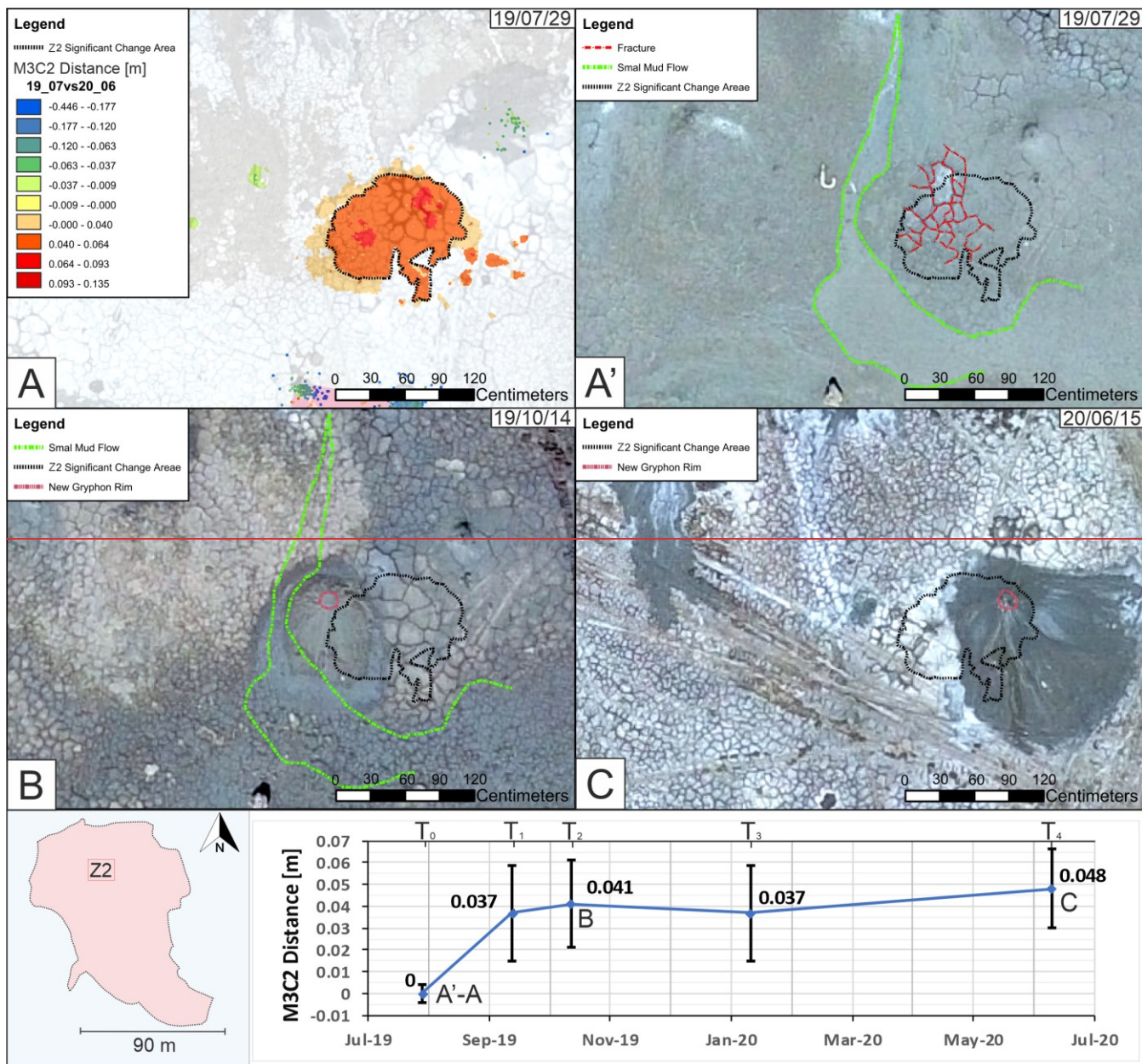
Figure 17: (A) M3C2 Distance (2019/07/29 VS 2020/06/15) of the Z2, the area used to create the time series is delimited with a dashed line (selected by significant change). (A') Orthophoto of 2019/07/29, the margin of the deflected flow, in green, and the radial fractures, in red. (B) Orthophoto of 19/10/14, formation of a new emission gryphon in red and the previous flow in green. (C) Orthophoto of 2020/06/15, formation of a new emission gryphon, in red. Below the time series with upward trend is shown. The reference system is WGS 84 / UTM zone 33N.

4. Discussion

UAV technology combined with SfM is a valuable tool in geological risk assessment and monitoring, however, some issues ~~questions~~ must be considered.

The first one is the quantity and quality of the acquired GCPs. According to the results, the minimum optimal number for geo-referencing is 12 GCPs. A slight improvement is observable up to 18 GCPs, while no appraisable improvement is detected for a higher number of GCPs (Fig.12). In addition, the method of acquiring GCPs reduces their error by using the Total Station Theodolite (Tab.1). The combined use of high-precision topographic instruments with an optimal number of GCPs improves the reliability of the datasets.

The second aspect to be considered is the evaluation ~~The second question is the evaluation~~ of distance uncertainty when two surveys are compared. The distance uncertainty between two data sets (surveys) can be considered as an estimate of the sensitivity of the methods to detect measurable topographic changes. The results of the M3C2-PM show that the average distance uncertainty between the first and the last surveys is about 6.5 cm over the whole area at the 95% confidence level (Fig.13-A). Furthermore, considering a smaller portion of the area, the uncertainty decreases to about 3.9 cm at the 95% confidence level (Fig.13-B). This allows us to analyse certain morphological changes and anthropogenic activity on the ~~volcano's~~ mud surface ~~shell~~ (Fig.14). The anthropogenic activity determined a height decrease of about 16 cm where a wood platform was previously located. As well as, a height increase of about 14 cm is recorded at the place where the wood platform has been relocated. The values recorded are consistent with the real thickness of the object detected, differing by 2 cm (Fig.14). The callipers show that it is possible to measure changes at least of 2 cm (Fig.11).

After ~~that~~ the uncertainty and sensitivity of the surveys were computed, the time series were made. Considering the significant changes and their errors, we computed the trend of deformation of two areas in order to reconstruct the evolution of the phenomena which generated these changes (Fig.16 and Fig.17).

Considering the results obtained by SfM, we propose a monitoring system of Santa Barbara mud volcano based on a semi-quantitative approach. We defined three states by setting a space-time range:

- Normal state if the deformation value does not exceed 5 cm in the range between 1 to 2 months.
- Pre-Alert state if the deformation value is between 5 cm and 10 cm during a period of between 1 to 2 months.
- Alert state if the deformation value exceeds 10 cm in the range between 1 to 2 months.

Obviously, these values must be considered in relation to the surface involved by deformation. To define the state of the activity of the mud volcano, the area affected by deformation must be a significant area of the total surface of the volcano. The definition of the activity is an important aspect of the monitoring of hazard, because there are many natural phenomena that can produce deformation in a little area (like a gryphon) or in a big area (like the sedimentation occurred at the border of the mud volcano), so the significant area affected by deformation must be correctly defined by an operator (public agency, university, institute of research or Dipartimento della Protezione Civile) which really knows the natural phenomena that can occur on the Santa Barbara mud volcano.

The methodological approach is valuable and efficient from the point of view of quantity and quality of data collected in relation to the work and time spent. This monitoring system of the deformations is a useful tool to detect the early unrest phase of the mud volcano usually induced by changes in pressure and volume of fluid raising from the stagnation chamber. The pre-eruptive deformation consists of a marked uplift and occasional small subsidence which are probably related to the redistribution of the subsoil of the pressurized fluids (Antonelli et al. 2014). According to Antonelli et al. (2014), soil uplifting can occur up to a year before the eruption.

5. Conclusion

In hazards management, ~~In the management of the hazard~~, the SfM technique ~~,~~ (Gomez et al., 2016, Kaab, 2000, Fugazza et al., 2018; Giordan et al., 2017, 2018) starts to be largely used by the scientific community. In the monitoring of potentially dangerous active sites, the UAVs are very advantageous because they are not used only as a support in the post-disaster events (Rokhmana and Andaru, 2017; Hisbaron et al., 2018), but also for the pre-event monitoring.

According to Kopf (2002), Antonelli et al., (2014), Madonia et al., (2011), INGV (2008a) and Regione Siciliana (2008), the deformations of the surface shell of mud volcanoes can occur up to one~~a~~ year before the paroxysmal event with doming and developing of structural lineaments with order of magnitude from centimetres to decimetres.

The results allow us to define the criteria for monitoring and analysing the study area. For the mud volcano of Santa Barbara, the monitoring criteria are:

- Monitoring interval between 1 and 2 months.
- The optimal number of GCPs is between 12 and 18.
- Acquisition of GCPs by high-precision topographical instrumentation (TST).
- The processing chain of the sparse point cloud according to workflow of USGS (2017) was enhanced by the correct value of "Tie Point Accuracy" and "Marker Accuracy" as suggested by James et al. (2017).
- An assessment of the state of activity of the mud volcano based on a semi-quantitative approach.

The frequencies of the campaigns depend on the status of activity, while the other criteria depend on the object / structure of the monitoring.

These criteria allow us to detect events with deformation of at least 2 cm. In the case of anomalous values ~~were~~ detected, the monitoring campaigns must be improved. This involves extensive monitoring, such as: i) developing time series localized in key areas, ii) combining different methodologies, e.g. micro-seismicity monitoring and three-dimensional geophysical prospecting (Imposa et al., 2016) to improve the monitoring system of the active geological process.

Acknowledgements

This paper was carried out with the financial support of the Presidenza del Consiglio dei Ministri (Project Code E98D19000000001, Monitoraggio e Studio dei Processi di Deformazione Superficiale Connessi al Vulcanismo-Sedimentario delle Maccalube di Santa Barbara (Caltanisetta) within the DPCM 25th May 2016 - Riqualificazione Urbana e la Sicurezza delle Periferie delle Città Metropolitane, dei Comuni Capoluogo e delle Città di Aosta, Scientific Supervisor: G. De Guidi). We thank Dr. Silvia Rita Popolo for her valuable support.

Finally, we are very grateful to the two anonymous referees who helped us to enhance the clarity and structure of the content of this manuscript.

References

Altamimi, Z., Collilieux, X. & Métivier, L.: ITRF2008: an improved solution of the international terrestrial reference frame, J Geod 85, 457–473, https://doi.org/10.1007/s00190-011-0444-4, 2011.

Amici, S., M. Turci, S. Giammanco, L. Spampinato, and F. Giulietti: UAV Thermal Infrared Remote Sensing of an Italian Mud Volcano. Advances in Remote Sensing 02.04, pp. 358–364. doi: 10.4236/ars.2013.24038, 2013a.

Amici, S., M. Turci, F. Giulietti, S. Giammanco, M. F. Buongiorno, A. La Spina, and L. Spampinato: Volcanic environments monitoring by drones mud volcano case study. ISPRS - International Archives of the Photogrammetry, Remote Sensing and Spatial Information Sciences XL-1/W2, pp. 5–10. doi: 10.5194/isprsarchives-xl-1-w2-5-2013, 2013b.

Andaru, R., and Rau, J.-Y.,: Lava dome changes detection at agung mountain during high level of volcanic activity using uav photogrammetry, Int. Arch. Photogramm. Remote Sens. Spatial Inf. Sci., XLII-2/W13, 173–179, https://doi.org/10.5194/isprs-archives-XLII-2-W13-173-2019, 2019.

Antonielli, B., Monserrat, O., Bonini, M., Righini, G., Sani F., Luzi, G., Feyzullayev, A. A., Aliyev, C. S.: Pre-eruptive ground deformation of Azerbaijan mud volcanoes detected through satellite radar interferometry (DInSAR), Tectonophysics, Volume 637, Pages 163-177, ISSN 0040-1951, https://doi.org/10.1016/j.tecto.2014.10.005, 2014.

Bakker, M. and Lane, S. N.: Archival photogrammetric analysis of river–floodplain systems using Structure from Motion (SfM) methods, Earth Surf. Proc. Land., 42, 1274–1286, https://doi.org/10.1002/esp.4085X, 2015.

Balaguer-Puig, M., Marqués-Mateu, Á., Lerma, J. L., and Ibáñez-Asensio, S.: Estimation of small-scale soil erosion in laboratory experiments with Structure from Motion photogrammetry, Geomorphology, 295, 285–296, https://doi.org/10.1016/j.geomorph.2017.04.035, 2017.

Bemis, S.P., Micklethwaite, S.,Turner,D., James, M.R., Akciz, S., Thiele, S. T., Ali Bangash, H.: Ground-based and UAV-Based photogrammetry: A multi-scale, high-resolution mapping tool for structural geology and paleoseismology, Journal of Structural Geology, Volume 69, Part A, Pages 163-178, ISSN 0191-8141, https://doi.org/10.1016/j.jsg.2014.10.007, 2014.

560   Boccardo, P., Chiabrando, F., Dutto, F., Tonolo, F.G., Lingua, A.: UAV deployment exercise for mapping purposes: evaluation of emergency response applications, Sensors: 15:15717–15737, https://doi.org/10.3390/s150715717, 2015.

Bonali, F.L., Tibaldi, A., Marchese, F., Fallati, F., Russo, E., Corselli, C., Savini, A.: UAV-based surveying in volcano-tectonics: An example from the Iceland rift, Journal of Structural Geology, Volume 121, Pages 46-64, ISSN 0191-8141, https://doi.org/10.1016/j.jsg.2019.02.004, 2019.

565   Bonini, M.: Mud volcanoes: Indicators of stress orientation and tectonic controls, Earth-Sci. Rev., 115, 121–152, doi:10.1016/j.earscirev.2012.09.002, 2012.

Bretar, F., Arab-Sedze, M., Champion, J., Pierrot-Deseilligny, M., Heggy, E., and Jacquemoud, S.: An advanced photogrammetric method to measure surface roughness: Application to volcanic terrains in the Piton de la Fournaise, Reunion Island, Remote Sens. Environ., 135, 1–11, https://doi.org/10.1016/j.rse.2013.03.026, 2013.

570   Brighenti, F., Carnemolla, F., Messina, D., Lupo, M., De Guidi, G. & Barreca, G.: Geo-referencing techniques of 3d models (SfM): Case study of mud volcano, Village Santa Barbara, Caltanissetta (Sicily), 89° Congresso SGI – SIMP, Geosciences for the environment, natural hazard and cultural heritage, Catania, 12-14 September, 2018.

Brunier, G., Fleury, J., Anthony, E. J., Gardel, A., and Dussouillez, P.: Close-range airborne Structure-from-Motion Photogrammetry for high-resolution beach morphometric surveys: Examples from an embayed rotating beach,
575   Geomorphology, 261, 76–88, https://doi.org/10.1016/j.geomorph.2016.02.025, 2016.

Carr, B. B., Clarke, A. B., Arrowsmith, J. R., Vanderkluysen, L., and Dhanu, B. E.: The emplacement of the active lava flow at Sinabung Volcano, Sumatra, Indonesia, documented by structure-from-motion photogrammetry, Journal of Volcanology and Geothermal Research, Volume 382, 2019, Pages 164-172, ISSN 0377-0273, https://doi.org/10.1016/j.jvolgeores.2018.02.004, 2018.

580   Casella, E., Rovere, A., Pedroncini, A., Mucerino, L., Casella, M., Cusati, L.A., Vacchi M., Ferrari M., Firpo M.: Study of wave runup using numerical models and low-altitude aerial photogrammetry: a tool for coastal management, Estuarine, Coastal and Shelf Science 149: 160–167, DOI:10.1016/j.ecss.2014.08.012, 2014.

Casella, E., Collin, A., Harris, D., Ferse, S., Bejarano, S., Parravicini, V., Hench, J. L., and Rovere, A.: Mapping coral reefs using consumer-grade drones and structure from motion photogrammetry techniques, Coral Reefs, 36, 269–275,
585   https://doi.org/10.1007/s00338-016-1522-0, 2016.

Castillo, C., Pérez, R., James, M.R., Quinton, N.J., Taguas, E.V., Gómez, J.A.: Comparing the accuracy of several field methods for measuring gully erosion. Soil Science Society of America Journal 76: 1319–1332, DOI:10.2136/sssaj2011.0390, 2012.

Catalano, S., De Guidi, G., Romagnoli, G., Torrisi, S., Tortorici, G., Tortorici, L.: The migration of plate boundaries in SE
590   Sicily: influence on the large-scale kinematic model of the African promontory in southern Italy, Tectonophysics, 449, pp. 41-62, 10.1016/j.tecto.2007.12.003, 2008.

De Beni, E., M. Cantarero, and A. Messina: UAVs for volcano monitoring: A new approach applied on an active lava flow on Mt. Etna (Italy), during the 27 February–02 March 2017 eruption. Journal of Volcanology and Geothermal Research 369, pp. 250–262. doi: 10.1016/j.jvolgeores.2018.12.001, 2019.

595   De Guidi, G., Brighent, F., Carnemolla, F., Imposa, S., Marchese, S. A., Palano, M., Scudero,S., Vecchio, A.: The unstable eastern flank of Mt. Etna volcano (Italy): First results of a GNSS-based network at its southeastern edge, Journal of Volcanology and Geothermal Research, ISSN: 0377-0273, Vol: 357, Page: 418-424, https://doi.org/10.1016/j.jvolgeores.2018.04.027, 2018.

De Guidi, G., Vecchio, A., Brighenti, F., Caputo, R., Carnemolla, F., Di Pietro, A., Lupo, M., Maggini, M., Marchese, S.,
600   Messina, D., Monaco, C., and Naso, S.: Brief communication: Co-seismic displacement on 26 and 30 October 2016 (Mw = 5.9 and 6.5) – earthquakes in central Italy from the analysis of a local GNSS network, Nat. Hazards Earth Syst. Sci., 17, 1885–1892, https://doi.org/10.5194/nhess-17-1885-2017, 2017.

Deng, F., Rodgers, M., Xie, S., Dixon ,T., H., Charbonnier, S., Gallant, E., A., Vélez C., M., L., Ordoñez, M., Malservisi, R., Voss, N. K., and Richardson, J., A.: High-resolution DEM generation from spaceborne and terrestrial remote sensing data
605   for improved volcano hazard assessment — A case study at Nevado del Ruiz, Colombia". Remote Sensing of Environment 233.111348. doi: 10.1016/j.rse.2019.111348, 2019.

Dewey, J. F., Helman, S., Knott, D., Turco, E. and Hutton, D. H. W.: Kinematics of the western Mediterranean, Geological Society, London, Special Publications, 45, 265-283, https://doi.org/10.1144/GSL.SP.1989.045.01.15, 1989.

Diefenbach, A., K., Adams, J., Burton, T., Koeckeritz, B., Sloan, J., and Stroud, S.: The 2018 U.S. Geological Survey-
610   Department of Interior UAS Kīlauea Eruption Response. AGU Fall Meeting Abstracts. Vol. 2018. AGU, V23D–0107, 2018.

Di Felice, F., Mazzini, A., Di Stefano, G., and Romeo, G.: Drone high resolution infrared imaging of the Lusi mud eruption. Marine and Petroleum Geology 90, pp. 38–51. doi: 10.1016/j.marpetgeo.2017. 10.025, 2018.

Dietrich, J. T.: Applications of structure-from-motion photogrammetry to fluvial geomorphology, PhD Thesis, 2014.

Dietrich, J. T.: Bathymetric Structure-from-Motion: extracting shallow stream bathymetry from multi-view stereo
615   photogrammetry, Earth Surf. Proc. Land., 42, 355–364, https://doi.org/10.1002/esp.4060, 2016/a.

Dietrich, J. T.: Riverscape mapping with helicopter-based Structure from-Motion photogrammetry, Geomorphology, 252, 144–157, https://doi.org/10.1016/j.geomorph.2015.05.008, 2016/b.

Eltner, A, Baumgart, P, Maas, HG, Faust, D.: Multi-temporal UAV data for automatic measurement of rill and interrill erosion on loess soil, Earth Surface Processes and Landforms 40: 741–755, DOI:10.1002/esp.3673, 2015.

620   Favalli, M., Fornaciai, A., Nannipieri, L., Harris, A., Calvari, S., and Lormand, C.: UAV-based remote sensing surveys of lava flow fields: a case study from Etna's 1974 channel-fed lava flows. Bulletin of Volcanology 80.29, pp. 1192–1196. doi: 10.1007/s00445-018-1192-6, 2018.

Federico, C., Liuzzo, M., Giudice, G., Capasso, G., Pisciotta, A., and Pedone, M.: Variations in CO2 emissions at a mud volcano at the southern base of Mt Etna: are they due to volcanic activity interference or a geyser-like mechanism?. Bulletin
625   of Volcanology 81.2. doi: 10.1007/s00445-018-1261-x, 2019.

660 Fonstad, M. A., Dietrich, J. T., Courville, B C., Jensen, J. L., Carbonneau, P. E.: Topographic Structure from Motion: A New Development in Photogrammetric Measurement, Earth Surface Processes and Landforms 38 (4): 421–430, doi:10.1002/esp.3366, 2013.

Fugazza, D., Scaioni, M., Corti, M., D'Agata, C., Azzoni, R. S., Cernuschi, M., Smiraglia, C., and Diolaiuti, G. A.: Combination of UAV and terrestrial photogrammetry to assess rapid glacier evolution and map glacier hazards, Nat. Hazards

665 Earth Syst. Sci., 18, 1055–1071, https://doi.org/10.5194/nhess-18-1055-2018, 2018.

Geoscience Australia: http://www.ga.gov.au/earthmonitoring/geodesy/auspos-online-gps-processingservice.html , 2011.

Gomez, C., Purdie, H.: UAV- based Photogrammetry and Geocomputing for Hazards and Disaster Risk Monitoring, Geoenviron Disasters 3, 23, https://doi.org/10.1186/s40677-016-0060-y, 2016.

Gomez-Gutierrez, A., Schnabel, S., Berenguer-Sempere, F., Lavado-Contador, F., Rubio-Delgado, J.: Using 3D photo-

670 reconstruction methods to estimate gully headcut erosion, Catena 120: 91–101, DOI:10.1016/j.catena.2014.04.004, 2014.

Giordan, D., Manconi, A., Remondino, F. & Nex, F.: Use of unmanned aerial vehicles in monitoring application and management of natural hazards, Geomatics, Natural Hazards and Risk, 8:1, 1-4, DOI:10.1080/19475705.2017.1315619, 2017.

Giordan, D., Hayakawa, Y., Nex, F., Remondino, F., and Tarolli, P.: Review article: the use of remotely piloted aircraft

675 systems (RPASs) for natural hazards monitoring and management. Natural Hazards and Earth System Sciences 18.4, pp. 1079–1096. doi: 10. 5194/nhess-18-1079-2018, 2018.

Greco, F., Giammanco, S., Napoli, R., Currenti, G., Vicari, A., La Spina, A., Salerno, G., Spampinato, L., Amantia, A., M. Cantarero, M., Messina, A., and Sicali, A.: A multidisciplinary strategy for in-situ and remote sensing monitoring of areas affected by pressurized fluids: Application to mud volcanoes: A multidisciplinary environmental monitoring strategy. 2016

680 IEEE Sensors Applications Symposium (SAS). IEEE. doi: 10.1109/sas.2016.7479861, 2016.

Harwin, S., Lucieer, A.: Assessing the Accuracy of Georeferenced Point Clouds Produced via Multi-View Stereopsis from Unmanned Aerial Vehicle (UAV) Imagery, Remote Sensing 4 (6): 1573–1599, doi:10.3390/rs4061573, 2012.

Heindel, R. C., Chipman, J. W., Dietrich, J. T., and Virginia, R. A.: Quantifying rates of soil deflation with Structure-from-Motion photogrammetry in west Greenland, Arct. Antarct. Alp. Res., 50, SI00012,

685 https://doi.org/10.1080/15230430.2017.1415852, 2018.

Hisbaron, D., R., Wijayanti, H., Iffani, M., Winastuti, R. and Yudinugroho, M.: Vulnerability mapping in Kelud volcano based on village information. IOP Conference Series: Earth and Environmental Science 148.012008. doi: 10.1088/1755-1315/148/1/012008, 2018.

Immerzeel, W., Kraaijenbrink, P., and Andreassen, L.: Use of an Unmanned Aerial Vehicle to assess recent surface elevation

690 change of Storbreen in Norway, The Cryosphere Discuss., https://doi.org/10.5194/tc-2016-292, 2017.

INGV: Comunicato sull'eruzione di fango in C.da Terrapelata-Santa Barbara (Cl) 11 Agosto 2008 — Aggiornamento del 16 Agosto, Istituto Nazionale di Geofisica e Vulcanologia, Sezione di Palermo (2008), (availble at http://www.pa.ingv.it/), 2008.

Imposa, S., Grassi, S., De Guidi, G., Battaglia, F., Lanaia, G., Scudero, S.: 3D Subsoil Model of the San Biagio 'Salinelle' Mud Volcanoes (Belpasso, Sicily) derived from Geophysical Surveys. Surv Geophys 37, 1117–1138. https://doi.org/10.1007/s10712-016-9380-4, 2016.

Imposa, S., Grassi, S., De Guidi, G., Patti, G., Brighenti, F., Carnemolla, F.: Geophysical and geodetic surveys for the characterization of the Santa Barbara mud volcano subsoil (Caltanissetta, Sicily): preliminary results. Conference: XXXVII Convegno Annuale Gruppo Geofisica della Terra Solida - sessione 3.2 "Geofisica applicata per le strutture superficiali e i rischi ambientali"At: Bologna - 19-21.11.2018, 2018

Jalandoni, A., Domingo, I., and Taçon, P. S. C.: Testing the value of low-cost structure-from-motion (SfM) photogrammetry for metric and visual analysis of rock art, Journal of Archaeological Science: Reports, 17, 605–616, https://doi.org/10.1016/j.jasrep.2017.12.020, 2018.

James, M.R., Robson, S.: Sequential digital elevation models of active lava flows from ground-based stereo time-lapse imagery, ISPRS Journal of Photogrammetry and Remote Sensing 97: 160–170, DOI:10.1016/j.isprsjprs.2014.08.011, 2014.

James, M.R., Varley, N.: Identification of structural controls in an active lava dome with high resolution DEMs: Volcán de Colima, Mexico, Geophysical Research Letters 39: L22303, DOI:10.1029/ 2012GL054245.L22303, 2012.

James, M. R., and Robson, S.: Straightforward Reconstruction of 3D Surfaces and Topography with a Camera: Accuracy and Geoscience Application, Journal of Geophysical Research: Earth Surface 117 (3): 1–17, doi:10.1029/2011JF002289, 2012.

James, M. R., Robson, S., d'Oleire-Oltmanns, S., Niethammer, U.: Optimising UAV topographic surveys processed with structure-from-motion: Ground control quality, quantity and bundle adjustment, Geomorphology, Volume 280, Pages 51-66, ISSN 0169-555X, doi.org/10.1016/j.geomorph.2016.11.021, 2017/a

James, M. R., Robson, S., Smith, M.W.: 3-D uncertainty-based topographic change detection with structure-from-motion photogrammetry: precision maps for ground control and directly georeferenced surveys, Earth Surf. Proc. Landforms, doi:10.1002/esp.4125, 2017/b.

James, M. R.: SfM-MVS PhotoScan image processing exercise, IAVCEI 2017 UAS workshop: Lancaster University, 2017.

James, M. R., Carr, B., D'Arcy, F., Diefenbach, A., Dietterich, H., Fornaciai, A., Lev, E., Liu, E. ., Pieri, D., Rodgers, M., Smets, B., Terada, A., von Aulock, F., Walter, T., Wood, K. and Zorn, E.: Volcanological applications of unoccupied aircraft systems (UAS): Developments, strategies, and future challenges, Volcanica, 3(1), pp. 67–114. doi: 10.30909/vol.03.01.67114, 2020.

Javernick, L., Hicks, D.M., Measures, R., Caruso, B., Brasington, J.: Numerical modelling of braided rivers with structure-from-motion derived terrain models, River Research and Applications 32: 1071–1081, DOI:10.1002/rra.2918, 2016.

Javernick, L., Brasington, J., Caruso, B.: Modeling the topography of shallow braided rivers using Structure-from-Motion photogrammetry, Geomorphology, Volume 213, Pages 166-182, ISSN 0169-555X, https://doi.org/10.1016/j.geomorph.2014.01.006, 2014.

Jia, M., Dawson, J.: AUSPOS: Geoscience Australia's online GPS positioning service, 27th International Technical Meeting of the Satellite Division of the Institute of Navigation, ION GNSS 2014, 1. 315-320, 2014.

Johnson, K., Nissen, E., Saripalli, S., Arrowsmith, J. R., McGarey, P., Scharer, K., Williams, P., Blisniuk, K.: Rapid mapping of ultrafine fault zone topography with structure from motion, Geosphere ; 10 (5): 969–986, doi: https://doi.org/10.1130/GES01017.1, 2014.

Kaab, A.: Photogrammetry for early recognition of high mountain hazards: New techniques and applications, Physics and Chemistry of the Earth, Part B: Hydrology, Oceans and Atmosphere, Volume 25, Issue 9, Pages 765-770, ISSN 1464-1909, https://doi.org/10.1016/S1464-1909(00)00099-X, 2000.

Kendra, J., Nissen, E., Saripalli, S., Arrowsmith, J.R., P McGarey, P., Scharer, K., Williams, P., Blisniuk, K.: Rapid Mapping of Ultrafine Fault Zone Topography with Structure from Motion, Geosphere 10 (5): 969–986, doi:10.1130/GES01017.1, 2014.

Lague, D., Brodu, N., Leroux, J.: Accurate 3D comparison of complex topography with terrestrial laser scanner: application to the Rangitikei canyon (N-Z), ISPRS Journal of Photogrammetry and Remote Sensing 82: 10–26, DOI:10.1016/j.isprsjprs.2013.04.009, 2013.

Lickorish, W. H., Grasso, M., Butler, R. W. H., Argnani, A., and Maniscalco, R.: Structural styles and regional tectonic setting of the "Gela Nappe" and frontal part of the Maghrebian thrust belt in Sicily, Tectonics, 18, 655–668, 1999,

Lucieer, A., de Jong, S.M., Turner D.: Mapping landslide displacements using Structure from Motion (SfM) and image correlation of multi-temporal UAV photography, Progress in Physical Geography 38: 97–116, DOI:10.1177/0309133313515293, 2014.

Madonia, P., Grassa, F., Cangemi, M., and Musumeci, C.: Geomorphological and geochemical characterization of the 11 August 2008 mud volcano eruption at S. Barbara village (Sicily, Italy) and its possible relationship with seismic activity, Nat. Hazards Earth Syst. Sci., 11, 1545–1557, https://doi.org/10.5194/nhess-11-1545-2011, 2011.

Marteau, B., Vericat, D., Gibbins, C., Batalla, R. J., and Green, D. R.: Application of Structure-from-Motion photogrammetry to river restoration, Earth Surf. Proc. Land., 42, 503–515, https://doi.org/10.1002/esp.4086, 2016.

Mercer, J. J. and Westbrook, C. J.: Ultrahigh-resolution mapping of peatland microform using ground-based structure from motion with multiview stereo, J. Geophys. Res.-Biogeo., 121, 2901–2916, https://doi.org/10.1002/2016JG003478, 2016.

Monaco, C. and Tortorici, L.: Clay diapirs in Neogene-Quaternary sediments of central Sicily: evidence for accretionary processes, J. Struct. Geol., Volume 18, Issue 10, Pages 1265-1269, ISSN 0191-8141, https://doi.org/10.1016/S0191-8141(96)00046-6, 1996.

Morgan, J. A., Brogan, D. J., and Nelson, P. A.: Application of Structure-from-Motion photogrammetry in laboratory flumes, Geomorphology, 276, 125–143, https://doi.org/10.1016/j.geomorph.2016.10.021, 2017.

Müller, D., Walter, T., R., Schöpa, A., Witt, T., Steinke, B., Gudmundsson, M., T., and Dürig, T.: High- Resolution Digital Elevation Modeling from TLS and UAV Campaign Reveals Structural Complexity at the 2014/2015 Holuhraun Eruption Site, Iceland. Frontiers in Earth Science 5. doi: 10.3389/feart.2017.00059, 2017.

Niethammer, U., James, M., Rothmund, S., Travelletti, J., and Joswig, M.: UAV-based remote sensing of the Super-Sauze landslide: Evaluation and results, Eng. Geol., 128, 2–11, https://doi.org/10.1016/j.enggeo.2011.03.012, 2012.

Pearson, E., Smith, M., Klaar, M., and Brown, L..: Can high resolution 3-D topographic surveys provide reliable grain size estimates in gravel bed rivers?. Geomorphology, 293, 143–155, https://doi.org/10.1016/j.geomorph.2017.05.015, 2017.

765   Piermattei, L., Carturan, L., de Blasi, F., Tarolli, P., Dalla Fontana, G., Vettore, A., and Pfeifer, N.: Suitability of ground-based SfMMVS for monitoring glacial and periglacial processes, Earth Surf. Dynam., 4, 425–443, https://doi.org/10.5194/esurf-4-425-2016, 2016.

Prosdocimi, M., Burguet, M., Di Prima, S., Sofia, G., Terol, E., Comino, J. R., Cerdà, A., and Tarolli, P.: Rainfall simulation and Structure-from-Motion photogrammetry for the analysis of soil water erosion in Mediterranean vineyards, Sci. Total

770   Environ., 574, 204–215, https://doi.org/10.1016/j.scitotenv.2016.09.036, 2017.

Regione Siciliana: Emergenza "Maccalube" dell'11 Agosto 2008 nel Comune di Caltanissetta,Descrizione dell'evento e dei danni, Regione Siciliana, Presidenza, Dipartimento della Protezione Civile, Servizio di Caltanissetta, Settembre 2008, p. 30 report available at: http://www.regione.sicilia.it/presidenza/protezionecivile/documenti/documenti.asp, 2008.

Rokhmana, C., A. and Andaru, R.: Some technical notes on using UAV-based remote sensing for post disaster assessment.

775   AIP Conference Proceedings.Vol. 1857. 1. AIP Publishing LLC. doi: 10 .1063/1.4987115, 2017.

Rosa, M., O'Brien, G., and Vermeiren, V.: Spain–UK–Belgium Comparative Legal Framework: Civil Drones for Professional and Commercial Purposes. Ethics and Civil Drones: European Policies and Proposals for the Industry. Ed. By M. de Miguel Molina and V. S. Campos. Springer International Publishing, pp. 43–75. doi: 10.1007/978-3-319-71087-7_4, 2018.

780   Russell, T. S.: Calculating the Uncertainty of a Structure from Motion (SfM) Model, Cadman Quarry, Monroe, Washington, University of Washington report available at: https://digital.lib.washington.edu/researchworks/bitstream/handle/1773/36262/Russell_MESSAGeReport030.pdf?sequence= 1&isAllowed=y, 2016.

Ryan, J.C., Hubbard, A.L., Box, J.E., Todd, J., Christoffersen, P., Carr, J.R., Holt, T.O., Snooke, N.: UAV photogrammetry

785   and structure from motion to assess calving dynamics at Store Glacier, a large outlet draining the Greenland ice sheet, The Cryosphere 9: 1–11, DOI:10.5194/tc-9-1-2015, 2015.

Saito, H., Uchiyama, S., Hayakawa, Y., S. and H., Obanawa: Landslides triggered by an earthquake and heavy rainfalls at Aso volcano, Japan, detected by UAS and SfM-MVS photogrammetry. Progress in Earth and Planetary Science 5.1. doi: 10.1186/s40645-018-0169-6, 2018.

790   Sapirstein, P. and Murray, S.: Establishing Best Practices for Photogrammetric Recording During Archaeological Fieldwork, J. Field Archaeol., 42, 337–350, https://doi.org/10.1080/00934690.2017.1338513, 2017.

Sapirstein, P.: Accurate measurement with photogrammetry at large sites, J. Archaeol. Sci., Volume 66, Pages 137-145, ISSN 0305-4403, https://doi.org/10.1016/j.jas.2016.01.002, 2016.

Sapirstein, P.: A high-precision photogrammetric recording system for small artifacts, J. Cult. Herit., 31, 33–45, https://doi.org/10.1016/j.culher.2017.10.011, 2018.

Seitz, L., Haas, C., Noack, M., and Wieprecht, S.: From picture to porosity of river bed material using Structure-from-Motion with Multi-View-Stereo, Geomorphology, 306, 80–89, https://doi.org/10.1016/j.geomorph.2018.01.014, 2018.

Serpelloni, E., Vannucci, G., Pondrelli, S., Argnani, A., Casula, G., Anzidei, M., Baldi, P., Gasperini, P.: Kinematics of the Western Africa-Eurasia plate boundary from focal mechanisms and GPS data, Geophysical Journal International, Volume 169, Issue 3, June 2007, Pages 1180–1200, https://doi.org/10.1111/j.1365-246X.2007.03367.x, 2007.

Smith, M.W., Quincey, D.J., Dixon, T., Bingham, R.G., Carrivick, J.L., Irvine- Fynn, T.D.L., Rippin, D.M.: Aerodynamic roughness of glacial ice surfaces derived from high-resolution topographic data, Journal of Geophysical Research - Earth Surface 121: 748–766, DOI:10.1002/ 2015jf003759, 2016.

Smith, M.W. and Vericat, D.: From experimental plots to experimental landscapes: topography, erosion and deposition in sub-humid badlands from Structure-from-Motion photogrammetry, Earth Surf. Proc. Land., 40, 1656–1671, https://doi.org/10.1002/esp.3747, 2015.

Snapir, B., Hobbs, S., and Waine, T.: Roughness measurements over an agricultural soil surface with Structure from Motion, ISPRS J. Photogramm., 96, 210–223, https://doi.org/10.1016/j.isprsjprs.2014.07.010, 2014.

Stöcker, C., Bennett, R., Nex, F., Gerke, M., and Zevenbergen, J.: Review of the Current State of UAV Regulations. Remote Sensing 9.5, p. 459. doi: 10 . 3390/rs9050459, 2017.

Tahar, K. M.: An evaluation on different number of ground control points in unmanned aerial vehicle photogrammetric block, ISPRS - International Archives of the Photogrammetry, Remote Sensing and Spatial Information Sciences, XL-2/W2. 93-98. 10.5194/isprsarchives-XL-2-W2-93-2013, 2013.

Turner, N. R., Perroy, R., L., and Hon, K.: Lava flow hazard prediction and monitoring with UAS: a case study from the 2014–2015 Pāhoa lava flow crisis, Hawaii. Journal of Applied Volcanology 6.17. doi:10.1186/s13617-017-0068-3, 2017b.

USGS: Unmanned Aircraft Systems Data Post-Processing, United States Geological Survey, UAS Federal Users Workshop 2017, https://uas.usgs.gov/pdf/PhotoScanProcessingDSLRMar2017.pdf, consulted at 30 of May2018, 2017.

Vinci, A., Todisco, F., Brigante, R., Mannocchi, F., and Radicioni, F.: A smartphone camera for the structure from motion reconstruction for measuring soil surface variations and soil loss due to erosion, Hydrol. Res., 48, 673–685, https://doi.org/10.2166/nh.2017.075, 2017.

Walter, T. R., Salzer, J., Varley, N., Navarro, C., Arámbula-Mendoza, R., and Vargas-Bracamontes, D.: Localized and distributed erosion triggered by the 2015 Hurricane Patricia investigated by repeated drone surveys and time lapse cameras at Volcán de Colima, Mexico. Geomorphology 319, pp. 186–198. doi: 10.1016/j.geomorph.2018.07.020, 2018.

Westoby, M.J., Brasington, J., Glasser, N.F., Hambrey, M.J., Reynolds, J.M., Hassan, M.A.A.M., Lowe, A.: Numerical modelling of glacial lake outburst floods using physically based dam-breach models, Earth Surface Dynamics 3: 171–199, DOI:10.5194/esurf-3-171-2015, 2015.

Westoby, M. J., Brasington, J., Glasser, N. F., Hambrey, M. J. and Reynolds, J. M.: Structure-from-Motion Photogrammetry: A Low-Cost, Effective Tool for Geoscience Applications, Geomorphology 179, Elsevier B.V.: 300–314, doi:10.1016/j.geomorph.2012.08.021, 2012.

830   Witt, T., Walter, T., R., Müller, D., Guðmundsson, M., T. and Schöpa, A.: The Relationship Between Lava Fountaining and Vent Morphology for the 2014–2015 Holuhraun Eruption, Iceland, Analyzed by Video Monitoring and Topographic Mapping. Frontiers in Earth Science 6. doi: 10 . 3389 / feart.2018.00235, 2018.

Woodget, A.S., Carbonneau, P.E., Visser, F., Maddock, I.P.: Quantifying submerged fluvial topography using hyperspatial resolution UAS imagery and structure from motion photogrammetry, Earth Surface Processes and Landforms 40: 47–64,

835   DOI:10.1002/esp.3613, 2015.

Zahorec, P., Papco, J., Vajda, P., Greco, F., M. Cantarero, M. and Carbone, D.: Refined prediction of vertical gradient of gravity at Etna volcano gravity network (Italy). Contributions to Geophysics and Geodesy 48.4, pp. 299–317. doi: 10.2478/congeo-2018-0014, 2018.